Nanoscale Advances

REVIEW

View Article Online
View Journal | View Issue

Cite this: *Nanoscale Adv.*, 2019, **1**, 4615

All-dielectric concentration of electromagnetic fields at the nanoscale: the role of photonic nanojets

Jinlong Zhu * and Lynford L. Goddard

The photonic nanojet (PNJ) is a narrow high-energy beam that was originally found on the back side of all-dielectric spherical structures. It is a unique type of energy concentration mode. The field of PNJs has experienced rapid growth in the past decade: nonspherical and even pixelized PNJ generators based on new physics and principles along with extended photonic applications from linear optics to nonlinear optics have driven the re-evaluation of the role of PNJs in optics and photonics. In this article, we give a comprehensive review for the emerging sub-topics in the past decade with a focus on two specific areas: (1) PNJ generators based on natural materials, artificial materials and nanostructures, and even programmable systems instead of conventional dielectric geometries such as microspheres, cubes, and trihedral prisms, and (2) the emerging novel applications in both linear and nonlinear optics that are built upon the specific features of PNJs. The extraordinary features of PNJs including subwavelength concentration of electromagnetic energy, high intensity focusing spot, and lower Joule heating as compared to plasmonic resonance systems, have made PNJs attractive to diverse fields spanning from optical imaging, nanofabrication, and integrated photonics to biosensing, optical tweezers, and disease diagnosis.

Received 8th July 2019
Accepted 9th November 2019

DOI: 10.1039/c9na00430k

rsc.li/nanoscale-advances

1. Introduction

We start the review without a detailed discussion of well-known underlying theories for photonic nanojets (PNJs) such as Mie scattering and index limitation. Instead, we organize the article with a viewpoint on the generation and application of PNJs with the hope of stimulating new directions for future research.

The nanoscale concentration of light in the visible and near-infrared (IR) spectral regions enables the re-examination of conventional rules for light–matter interactions and thus, lies at the heart of revolutionary photonic devices. The most well-known demand for nanoscale concentration of light undoubtedly comes from the semiconductor industry. Because of their

Photonic Systems Laboratory, Department of Electrical and Computer Engineering, University of Illinois at Urbana-Champaign, 208 N. Wright St., MNTL 2231, Urbana, IL 61801, USA. E-mail: zhuwdwz1@illinois.edu

Dr. Jinlong Zhu obtained his B.Sc. and PhD in Mechatronic Engineering from Huazhong University of Science and Technology, Wuhan, China. He is presently working at the Department of Electrical and Computer Engineering at the University of Illinois at Urbana-Champaign as a Post-Doctoral researcher. His research interests involve optical metrology, nanoscale sensing, semiconductor defect inspection, chiral photonics, integrated photonics, inverse problem, and topology optimization. He is co-author of over 50 publications and 10 patents.

Lynford Goddard is a professor of Electrical and Computer Engineering at the University of Illinois. His group fabricates, tests, and models photonic sensors, circuits, and instrumentation, develops novel device processing techniques, and applies quantitative phase microscopy for nanoscale science and for semiconductor wafer metrology. He received the Presidential Early Career Award for Scientists and Engineers (PECASE) in 2010 and the AAAS Early Career Public Engagement Award in 2011. He is co-author of over 200 publications and 12 patents.

wider bandwidth, photonic devices can replace electronic devices provided they can be densely integrated.[1] However, delivering electromagnetic energy through conventional photonic devices (*e.g.*, optical waveguides and photonic crystals) in a volume comparable to that of electronic devices manufactured at advanced technology nodes is non-trivial. Specifically, electromagnetic waves with the vacuum wavelength λ cannot last long in a dielectric cavity of characteristic size smaller than $\lambda/2n$, because the self-sustaining oscillations (*i.e.*, the balance in the potential energy transfer) between the electric field energy and magnetic field energy of electromagnetic waves cannot be supported in the cavity.[2] This phenomenon can be more briefly understood as the fundamental diffraction limit of light.

However, if we introduce free carriers in the cavity, the potential energy can also be stored in the form of kinetic energy of free carriers, making it possible to restore the balance of energy transfer. This is the physical fundament of why visible and IR light can be concentrated into regions with nanoscale characteristic sizes using metallic objects. Without any doubt, the research on plasmon-assisted concentration of light into nanoscale volumes will remain as one of the hot fields (along with metamaterials) because of its revolutionary potentials in many fields like microscopy,[3] sensing,[4,5] and integrated circuits.[6] By propagating a mid-IR surface wave along a tapered two-wire transmission line, nanoscale IR spot with a diameter of 60 nm ($\lambda/150$) was observed using a nearfield microscope.[7] Nanoscale focusing with a 2×5 nm^2 footprint and an intensity enhancement of 3.0×10^4 was achieved in an Au–SiO_2–Au gap plasmon waveguide using a carefully engineered three-dimensional taper.[8] Im *et al.* described a high-throughput, label-free plasmonic exosome assay for quantitative analysis of exosomes.[9] Liu *et al.* introduced a far-field optical superlens capable of imaging beyond the diffraction limit *via* converting the evanescent waves into propagating waves, which can be measured in the far field.[10] However, although surface plasmon polaritons of metallic structures (especially Au and Ag, whose scattering rate are 12.32×10^{13} s^{-1} and 3.6×10^{13} s^{-1}, respectively) have been conceptually applied to create many novel devices or to boost the performance of existing mechanisms, the extremely high-loss in metallic materials typically makes high-efficiency plasmonic-based photonic devices impractical. The few exceptions have been in imaging and sensing, where sensitivity is more critical than efficiency. A highly doped semiconductor is a promising alternative to metals, but ω_p for a semiconductor is an order of magnitude lower, thereby limiting them to the mid-IR and longer wavelengths.[2,11] Gain materials to compensate metal loss have been researched, but theoretical computations show that extremely high power is required. For those reasons, in recent years, interest has grown in using non-metallic, all-dielectric materials to pull off some of the same light-localization tricks enabled by plasmonics while avoiding the tendency of plasmonic systems to dissipate optical energy as heat.[12]

The trick in all-dielectric light concentration at the nanoscale is that although light cannot be squeezed in a subwavelength cavity, it can be tailored in all three dimensions outside of dielectric structures *via* the contribution from evanescent waves or *via* purely the interference of propagating waves.[13] More importantly, nanostructured dielectric materials with a high value of the refractive index offer a novel way to directly engineer a magnetic field response at optical frequencies in addition to the electric field response in plasmonic structures. These features of dielectric nanostructures have recently risen to prominence in the nanophotonics toolkit for diverse fields by creating electric or magnetic hot spots. Albella *et al.* investigated the possibility of utilizing the field-enhancement in the nanogap of silicon dimers for the fluorescence of either electric or magnetic emitters.[14] Shcherbakov *et al.* demonstrated ultrafast all-optical switching in subwavelength nonlinear dielectric nanostructures exhibiting localized magnetic Mie resonances.[15] Regmi *et al.* demonstrated the effectiveness of an approach using the field hot spots created by silicon dimers to enhance the fluorescence detection of single molecules.[16] The creation of nanoscale hot spots through the engineering of dielectric nanostructures in the near-field region arises from the interference and diffraction nature of various components of light (especially the evanescent ones); thus, an interesting way to create deep subwavelength hot spots in the far-field *via* the propagating components only, is based on superoscillation theory,[17–19] which has been successfully applied into the area of super-resolution imaging. Although the aforementioned metasurfaces are capable of tailoring the light field for nanoscale localization or focusing either in the near-field or far-field, the complicated processes required in the fabrication of metasurfaces hinder the generalization and industrialization for diverse applications. One may ask, are there any nanostructures that behave similar to metasurfaces in terms of squeezing the light but have much simpler geometrical profiles? Actually, we do have, and the answer is quite straightforward, *i.e.* the slot waveguides.[20] A slot waveguide can guide strongly confined light in the nanoscale low refractive index gap by total internal reflection. The underlying physics, *i.e.*, the discontinuity of the electric field (*E*-field) at high-refractive-index-contrast interfaces,[21] can be somehow related to the physical fundaments of the hot spots created in the nanoscale dimers.[15] However, the realization of nanometer scale localization of electromagnetic fields pays the price of rigid excitation conditions (*i.e.*, fiber-coupled laser coupling or grating-based coupling) and long transverse length. For all those reasons, we do need a type of simple, non-metallic, massively manufacturable, and small-in-dimension structures that concentrates light to nanoscale volumes for various types of excitation mechanisms including free-space beams and fiber or waveguide-coupled modes.

Surprisingly, the natural world has provided us the answer: spheres, which are the most universal and simple geometries in nature and can be found from celestial bodies to atoms, can meet all the rigid conditions as mentioned earlier when they interact with light: microscale or even nanoscale dielectric spheres with the refractive index smaller than two, can concentrate free-space beams or waveguide modes impinging from any spatial direction to deep subwavelength volumes. Actually, it's been known since ancient times that a garden

should not be watered in the afternoon, as the small droplets of water deposited on the leaves could cause sunburns.[22] Yet, the thorough investigation of the narrow, non-resonant, and highly spatially confined optical field emerging on the shadow side surface of microspheres with diameters comparable to or somewhat larger than the wavelength of the incident optical radiation, was not implemented until 2004, when Chen *et al.* coined the terminology "photonic nanojet" for the concentrated field. Although microspheres do have similar geometrical features with those of a macroscopic lens or a conventional micro-lens, the rigorous analysis through Mie theory combined with Debye series have demonstrated that the behavior of the microsphere is significantly different from that of the conventional solid immersion lens in terms of the beam width, concentrated energy, and reaction to nanoscale perturbations.[23,24] Such a difference can be somehow attributed to the size effect: microspheres that could generate PNJs, typically have the size in between Rayleigh particles and micro-lens; thus, one can use neither electrostatic approximation nor geometrical optics, but only the Mie scattering theory, to analytically disclose the underlying physics, in which, the unusual entanglement of propagating and evanescent components may be responsible for the uniqueness of PNJ properties.[25] Here, we use the term "may be" because the underlying physics of some PNJ-based applications is still under debate, *e.g.*, the PNJ-assisted super-resolution imaging,[26] though there are already considerably numerical and experimental investigations.[27–31] However, the mystery in the physics did not hinder the formation of a huge family of applications based on PNJs—we can now find the footprints of the PNJ in nearly all the major subjects related to nanophotonics, *e.g.*, nanolithography, nanoscopy, fluorescence enhancement, sensing, photodetection, resonators, Raman and Stokes microscopy, optical data storage, transmission enhancement, waveguides, and all-dielectric switching. Although the term "PNJ" was originally coined for the concentrated beam regarding microspheres, it has been generalized immensely to also represent the squeezed field on the shadow surface of non-spherical objects, such as cuboids, triangles, gratings, and nanofiber assemblies.[32–35] Such a generalization facilitates the explanation and description of the light–matter interaction for non-spherical objects in the PNJ language. The emergence of novel light sources including frequency combs,[36] ultra-fast lasers,[37] super-continuum sources,[38] and quantum atom-fiber photonics,[39] provide a brand-new dimension for the PNJ generators (microsphere and its derivatives) to manipulate light–matter interaction in extreme environments. For all these reasons, we do believe that the PNJ, which is promising in many fields in terms of efficiency, simplicity, manipulability, and manufacturability, will remain as an interesting and hot research topic. Hence, we do feel, a thorough review for disclosing new perspectives, unusual physics, and exciting trends, is of great importance to both new entrants in the field and people who are seeking to use it in interdisciplinary work. We should mention that different from previous review articles by Wang and Heifetz that primarily discuss PNJs formed by dielectric particles such as microspheres, microcylinders, and prisms,[21,23] this article is more focused on disclosing the diversity in PNJ generators for both nature-inspired and metamaterials-based ones, as well as on the emerging novel applications of PNJs in both linear and nonlinear regimes in the past decade. The techniques (including index engineering, geometry engineering, and topology optimization) disclosed in Sec. 2 enables the customization of PNJ properties including FWHM, energy concentration, gradient field, and microlensing effects. The capability of customizing these properties of PNJ is critical to diverse applications of PNJs because each application requires one or several specific properties of PNJs.

2. Diversity in PNJ generators

2.1 Origin and theory of PNJs

The initial identification of the PNJ for a dielectric cylinder and a dielectric sphere was reported by Chen and Li, respectively.[40,41] Applying a high-resolution finite-difference time-domain (FDTD) computational solution of Maxwell's equations or an exact eigenfunction series solution of Maxwell's equations in spherical coordinates (*i.e.*, Mie theory), evidence was provided that both dielectric cylinders and spheres with microscale dimensions illuminated by a plane wave, can generate a narrow, high-intensity, sub-diffraction-waist beam (*i.e.*, the PNJ) that propagates into the background medium from the shadow-side surface. By analogy with macroscopic components like cylindrical lenses and spherical lenses that are characterized by the geometrical optics, microscale cylinders and spheres theoretically concentrate plane waves with specific polarization states into a line and a point, respectively. Consider now such a cylindrical or spherical lens having a small but fixed f-number and shrinking down its dimensions to the microscale such that its focal length f becomes smaller than a fraction, a, of the wavelength λ, *i.e.*,

$$f < a\lambda. \tag{1}$$

See the schematics in Fig. 1. When eqn (1) applies, the evanescent components of the scattering field cannot be neglected as can be done with macroscopic optics components. At a distance of λ/e, from the microlens, the power of the evanescent waves attenuates to 36.8% of its peak value. Moreover, for the scattering of visible and near-IR light *via* microscale objects, eqn (1) is usually much tighter than the inequality that relates to the Fraunhofer distance

$$f < 2D^2/\lambda, \tag{2}$$

where D is the greatest width of the scattering object. This indicates that the characteristics of the diffraction pattern after passing through the microscale objects include: (i) that the fringes become more pronounced, (ii) that the diffraction pattern changes in structure as the distance f is increased, and (iii) that the phase change in the region governed by eqn (2) is not linear. Because of the existence of evanescent components and the nature of diffraction at the scale comparable to the wavelength, the actual focal length and the concentration

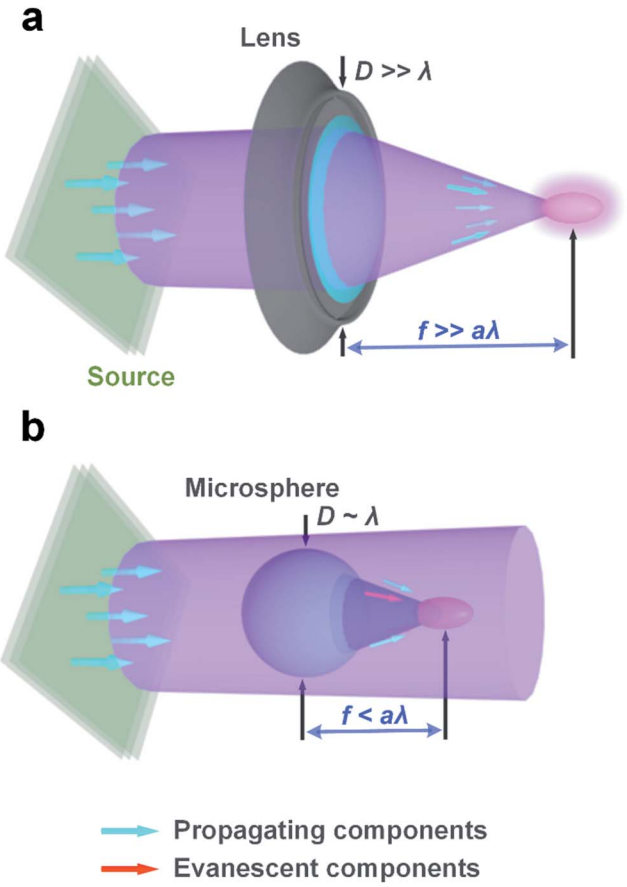

Fig. 1 Schematics of the concentration for the plane-wave excitation based on (a) macroscale and (b) microscale objects. The ideal focal lengths shown in (a) and (b) are far larger and smaller than the wavelength, respectively.

feature for impinging waves behave vastly different than that of conventional optics components. Using Mie theory, we can easily determine which specific modes contribute the most to the formation of PNJs, but one should note, again, that the unusual features (*e.g.*, the sub-diffraction waist) of PNJs intrinsically arise from the size-effect-induced light diffraction and mixing of the evanescent and propagating components. An interesting topic, therefore, is understanding the physics of how the diffraction aperture and the combination of evanescent and propagating components contribute to specific features of the PNJ, *e.g.*, the beam waist, the concentrated energy, and the working distance. Although disclosing the underlying physics analytically is only feasible for simple geometries, there have been some attempts of using quasi-analytical models or complicated theories to understand the PNJ.[42–45] However, the majority of PNJ engineering is still based on numerical and optimization algorithms because of their simplicity and maturity and the ubiquity of high-performance computing. We will next give a review on designing PNJ generators from five different perspectives: natural PNJ generators, index engineering, geometry engineering, non-conventional designs, and a generalized design framework.

2.2 PNJ generators in the nature

Theoretically, any spherical or cylindrical micro-object with the refractive index smaller than two can be a PNJ generator.[21] Many building blocks of living organisms such as proteins, water, and carbohydrates have indices less than two in the visible regime (this is also the reason why the Born or Rytov approximation can be introduced to enable optical phase imaging for living cells without suffering from significant multiple scattering).[46] This makes it possible to utilize natural materials to generate PNJs.[47] It has been demonstrated that spider silk with a spherical cross-section can behave as a superlens for super-resolution imaging in contact mode at $\lambda/6$ scale, which is well beyond the classical limit [see Fig. 2(a)].[48] It has been suggested that the phototaxis of Synechocystis cells may arise from the spherical microlens effect of the cells.[49] In a macroscale imaging system, a high-NA objective lens enables optical trapping and sensing of nanoscale objects.[50,51] Analogously, the microlens effect of cells make it possible to use a single cell to trap, image, and sense nanoparticles as was successfully demonstrated very recently.[52] A significant difference to conventional optical imaging is that the single cell can be operated in contact mode such that the possible evanescence–propagation coupling can facilitate super-resolution imaging. See Fig. 2(b) showing the focusing effect of a single cell for red, green, blue (RGB) lasers and nanopattern imaging in scanning mode. In the field of optical tweezers, self-bonding is a phenomenon in which a cascade of objects forms as the result of the generation of a trapping potential through the trapped objects. A cell trapped at the tip of fiber concentrates the electromagnetic energy and forms a trapping potential to capture a second cell. "Chain reaction" form such that more and more cells become trapped until the trapping potential can no longer overcome the background perturbation. Such a phenomenon has been reported in several studies such as biophotonic waveguides, enhanced upconversion fluorescence, and near-field optical probing.[46,53–55] See a bio-microlens trapped at the tip of a fiber that behaves as a PNJ generator to form a *E. coli* chain in Fig. 2(c). An interesting topic is how to achieve a tunable "biolens" such that its optical features match diverse applications. It has been shown that the red-blood-cell-based microlens can stretch the cell membrane with an enhancement factor of 1.5 in a noncontact and noninvasive manner.[56] This enlightens the possibility of using a second PNJ to tune the geometric shape of a cell in order to achieve an adjustable biolens. A more straightforward method is to control the liquid buffer's chemistry such that the red blood cell can swell up from a disk shape to a sphere, leading to a varying focal length.[57] As cells are typically operated in liquids, the aforementioned tunable techniques are limited to immersion environments.[58] Moreover, the precise control over a biolens is challenging because a living microlens has diverse fundamental elements and thus its accurate optical response to external excitation is nonlinear and unknown.[59] For these reasons, we will focus on the artificial-materials-based PNJ generators thereinafter. However, we should mention that the biolens will still find its unique value in many applications

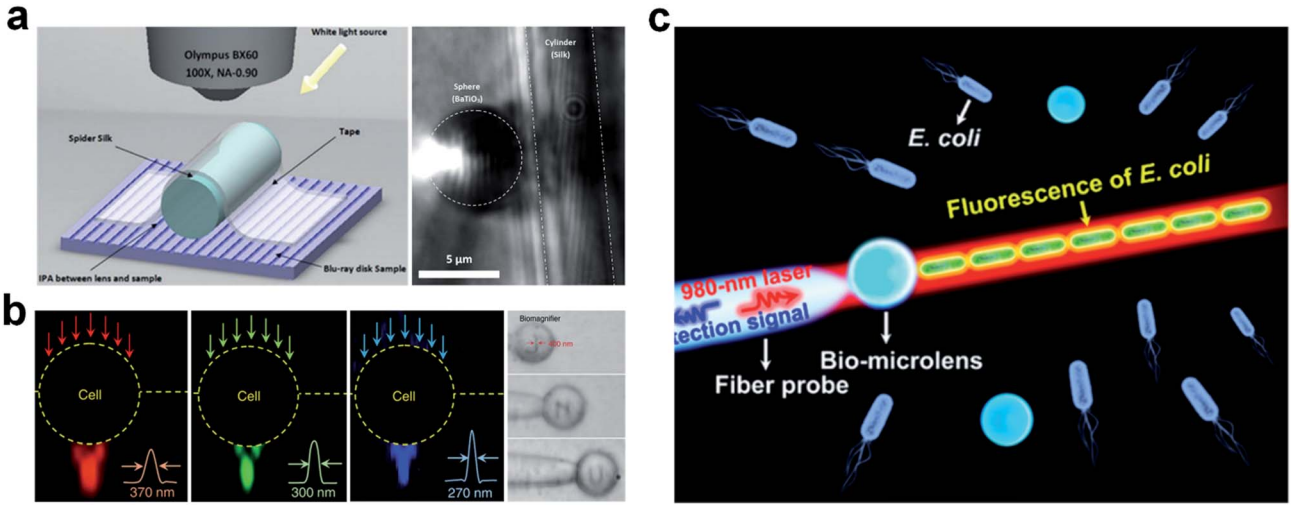

Fig. 2 (a) Schematic diagram of silk biosuperlens imaging and super-resolution images of a Blu-ray disk in reflection mode. Reproduced with permission from ref. 48. Copyright 2016, American Chemical Society. (b) Darkfield images showing the focusing effect of a single cell for RGB lasers. Reproduced with permission from ref. 52. Copyright 2019, Nature Publishing Group. (c) Schematic showing the fluorescence enhancement of an *E. coli* chain originating from a bio-microlens. Reproduced with permission from ref. 53. Copyright 2017, American Chemical Society.

where man-made materials can hardly be applied, such as intravital trapping and sensing.

2.3 Index engineering for PNJs

The refractive index determines the angle of refraction on an interface *via* the generalized Snell's law;[60,61] thus, the most direct way to tune PNJs is *via* controlling the index of the PNJ generators. It has been shown numerically, as early as the year 2009, that a radially index-graded microsphere can increase the useful length of a PNJ by an order-of-magnitude to approximately 20 wavelengths, which is effectively a quasi-one-dimensional light beam. This may be useful for optical detection of naturally or artificially introduced nanostructures deeply embedded within biological cells.[62] Actually, by analogy with macroscopic spherical lenses, one can anticipate, qualitatively, that reducing the index contrast between the microsphere and its surrounding ambient could longitudinally elongate the hot spot; however, rigorous numerical modelling is required to quantitatively validate the prediction because of the evanescent contribution and effects of diffraction.[63] Two-dimensional and three-dimensional spherical microstructures are the most widely investigated objects for index engineering. Geints *et al.* considered dielectric spherical composite particles consisting of a core and several concentric shells having different refractive indices. The dependence of the longitudinal and latitudinal sizes of a PNJ and the PNJ's peak intensity on the optical contrast variation of the shells was numerically investigated. They showed that by properly changing the refractive indices of neighboring shells, it is possible to manipulate the PNJ shape and, particularly extend its longitudinal size or increase its peak intensity.[64] Shen *et al.* showed that ultralong nanojets can be generated using a simple two-layer microsphere structure. In particular, they showed that for a glass-based two-layer microsphere, the PNJ has an extension of 22 wavelengths.[65] A similar investigation of a liquid-filled hollow microcylinder under a liquid immersion condition was numerically investigated by Gu *et al.*, in which they demonstrated super-long PNJs with decay lengths more than 100 times the illumination wavelengths in the outer near-field region of the microcylinder.[66] Zhen *et al.* reported the realization of an ultranarrow PNJ, which is formed by a two-layer microcylinder of high refractive-index materials. They numerically showed that under 632.8 nm illumination, the full width at half maximum (FWHM) of the beam waist can reach 87 nm ($\sim\lambda/7.3$), which appears to be the narrowest PNJ ever reported.[67]

In fact, tuning the scattering by varying index contrast has a long history (for instance, the Luneburg lens,[68] which is widely employed at microwave frequencies). But, what really makes the community excited is the capability of dynamically varying the index contrast for tuning the properties of PNJs, so that a single device can satisfy the needs of diverse applications. Possibly, the easiest and also the most direct way to tune is through liquid crystals (LCs). LCs have been extensively utilized in many fields including organic electronics and energy conversion, the creation of nanostructured materials or ordering nano- and microparticles, actuators, polymer-dispersed LCs, and spatial light modulators.[69–73] Liu *et al.*,[74] Matsui *et al.*,[75] Eti *et al.*,[76] and Du *et al.*,[77] have investigated the properties of PNJs as functions of the phase transitions of LCs, but the first experimental imaging of tunable PNJs using LC control appears to have been achieved by Matsui and Tsukuda.[78] In their experiments, a LC microdroplet formed in a polydimethylsiloxane (PDMS) matrix is sandwiched between indium-tin-oxide (ITO) electrodes. Applying external voltage to the device alters the alignment of the LC molecules [a nematic LC (E7, LCC)] in the droplet, which changes the effective refractive index, and thus the electro-tuning of the PNJ can be realized. See the schematic of the

PNJ generator device in Fig. 3(a) and (b), and the reconstructed PNJ generated by a LC microdroplet under applied voltage viewed along the optical z axis, as measured by a confocal microscope. The three plots from top to bottom on the right-hand side of Fig. 3(c) represent the beam width, beam length, and intensity enhancement of the PNJ as a function of applied voltage, respectively.

The phase transition of LCs is not the only way to tune the properties of PNJs, but any other methods that modify the index distribution would work as well. For instance, phase change materials[79–83] switch from their amorphous state to their crystalline state and *vice versa*. This provides a binary tuning of the index contrast. Soh *et al.* implemented a numerical investigation of how temperature can tune the FWHM and working distance (WD) of a PNJ generated by a glass microsphere whose top half-surface is coated with vanadium oxide (VO_2), a phase change material.[84] See the schematic in Fig. 3(d). As VO_2 changes from semiconducting to metallic phase, the refractive index of the VO_2 layer changes at its transition temperature of 68 °C. They found that a coating of 75 nm on a 5.0 μm diameter microsphere with a refractive index of 1.50 is optimal, as it tunes the FWHM the greatest while remaining thin enough to have a high transmission. When the temperature is raised from 20 °C to 90 °C, the FWHM varies from 0.43 μm to 0.37 μm, corresponding to a 14.0% change. The WD varies from 0.29 μm to 0.20 μm, corresponding to a 31.0% change. To enable the dynamic tuning of PNJs, one needs a reversible mechanism that facilitates the variation of indices in a continuous space. It has been demonstrated that the refractive index and optical band gap of CR-39 polymers in UV-visible range reduce as the annealing temperature increases,[85] making it possible to use CR-39 polymer as the scaffold to design PNJ generators with tunable features *via* heating. Different to heat tuning, Yu *et al.* reported that the refractive index of transition metal dichalcogenide monolayers, such as MoS_2, WS_2, and WSe_2, can be substantially tuned (by >60% in the imaginary part and >20% in the real part) around exciton resonances using complementary metal–oxide–semiconductor (CMOS) compatible electrical gating.[86] However, the aforementioned mechanisms only work for specific materials and cannot be generalized to arbitrary ones because of different electro-optic and thermal-optic coefficients. The nonlinear optical effect is an inherent attribute of materials. Laser light with sufficiently strong power can result in a nonlinear response of a material system, *i.e.*,

$$P(t) = \varepsilon_0\chi^{(1)}E(t) + \varepsilon_0\chi^{(2)}E^2(t) + \varepsilon_0\chi^{(3)}E^3(t) + \ldots, \quad (3)$$

where $P(t)$ and $E(t)$ are the dielectric polarization density and electrical field at time t, respectively. The coefficients $\chi^{(n)}$ are the n-th-order susceptibilities of the material. Here, we propose that in theory, we could use the nonlinear optical response of

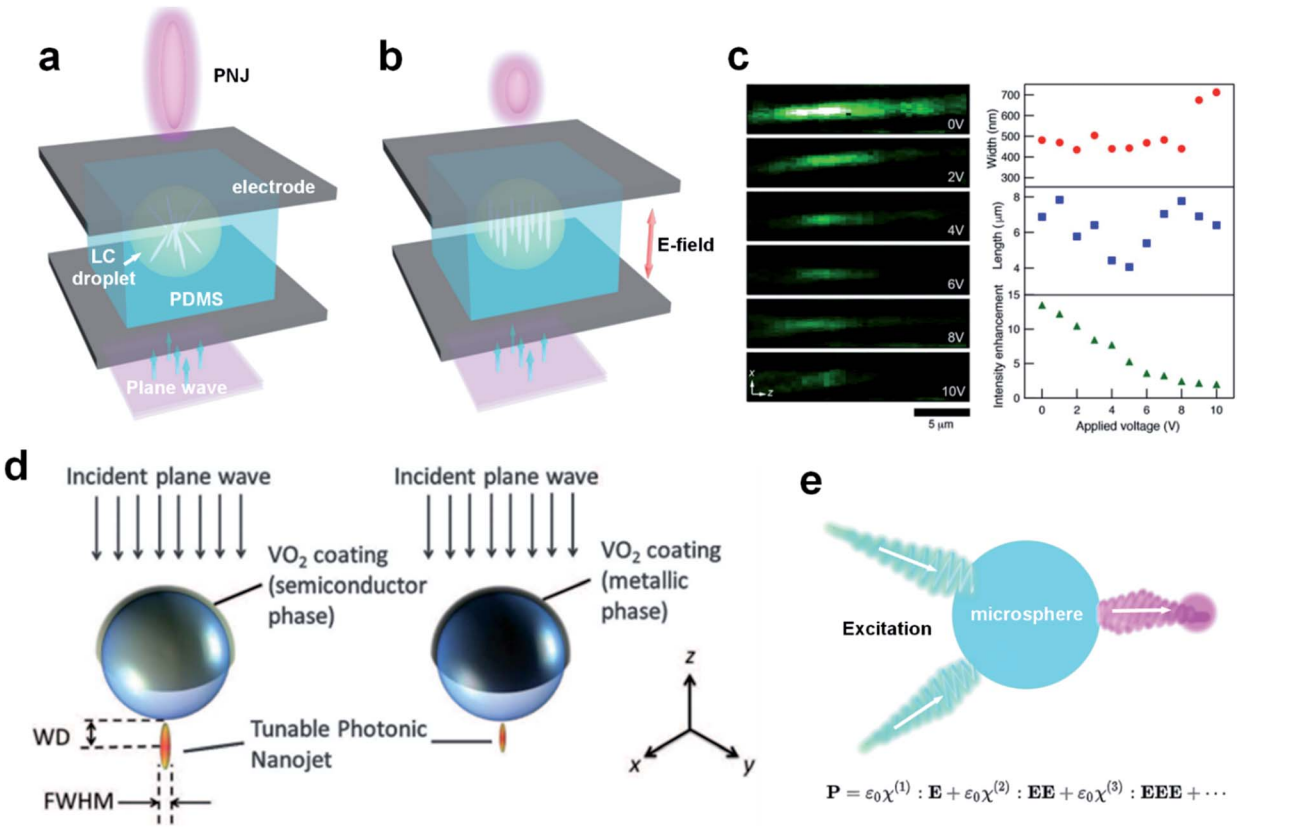

Fig. 3 Schematic of tunable PNJ generator device with (a) off and (b) on states based on a LC microdroplet and (c) measured PNJ under different voltages viewed along the z axis. Reproduced with permission from ref. 78. Copyright 2017, Optical Society of America. (d) Schematic diagram showing the VO_2-coated microsphere for 800 nm illumination. Reproduced with permission from ref. 84. Copyright 2016, Optical Society of America. (e) Our proposal for generating a tunable PNJ using nonlinear effects in a dielectric microsphere.

dielectric materials to tune PNJs; see the schematic in Fig. 3(e). But we should mention that, achieving the large range of input power necessary for tuning will be challenging as is the case for thermal or electrical tuning. LCs currently seem the most practical approach for energy-efficient tunable PNJs but future research into the reversible tuning of dielectric materials (*e.g.*, SiO_2, Si_3N_4, and polymers) may yield new solutions.

2.4 Geometry engineering for PNJs

Compared to index engineering, the customization of shapes for diverse PNJ applications is much easier to implement, owing to, at least partially, the advances in nanoscale fabrication.[87–91] One typical advantage of geometry engineering is that the limitation of low-index materials (refractive index less than two) as required in conventional dielectric microspheres, can be conquered;[92] however, the majority of PNJ generators use aspherically-shaped low-index materials (possibly, due to convention). The second reason for the bloom of geometry engineering is related to circumventing the drawbacks of PNJs generated by microspheres and microcylinders for specific applications.[93] For example, to detect intrinsic nanostructures and artificially introduced nanoparticles that are deeply embedded within biological cells researchers requires a long PNJ length, whereas a rapidly convergent PNJ generated by the microsphere or microcylinder is followed by a fast divergence.[77] We give, herein, a review on the major published results of the past decade on the geometry engineering for PNJs, to remind our readers of the diversity in PNJ customization.

Geints *et al.* investigated the longitudinal and transverse dimensions of the PNJ as well as the dependence of its peak intensity on the optical contrast of micrometer-sized composite particles consisting of a nucleus and several shells with different refractive indices. It was shown that, the length and peak intensity of PNJs can be manipulated *via* varying the index contrast.[94] Grojo *et al.* showed both numerically and

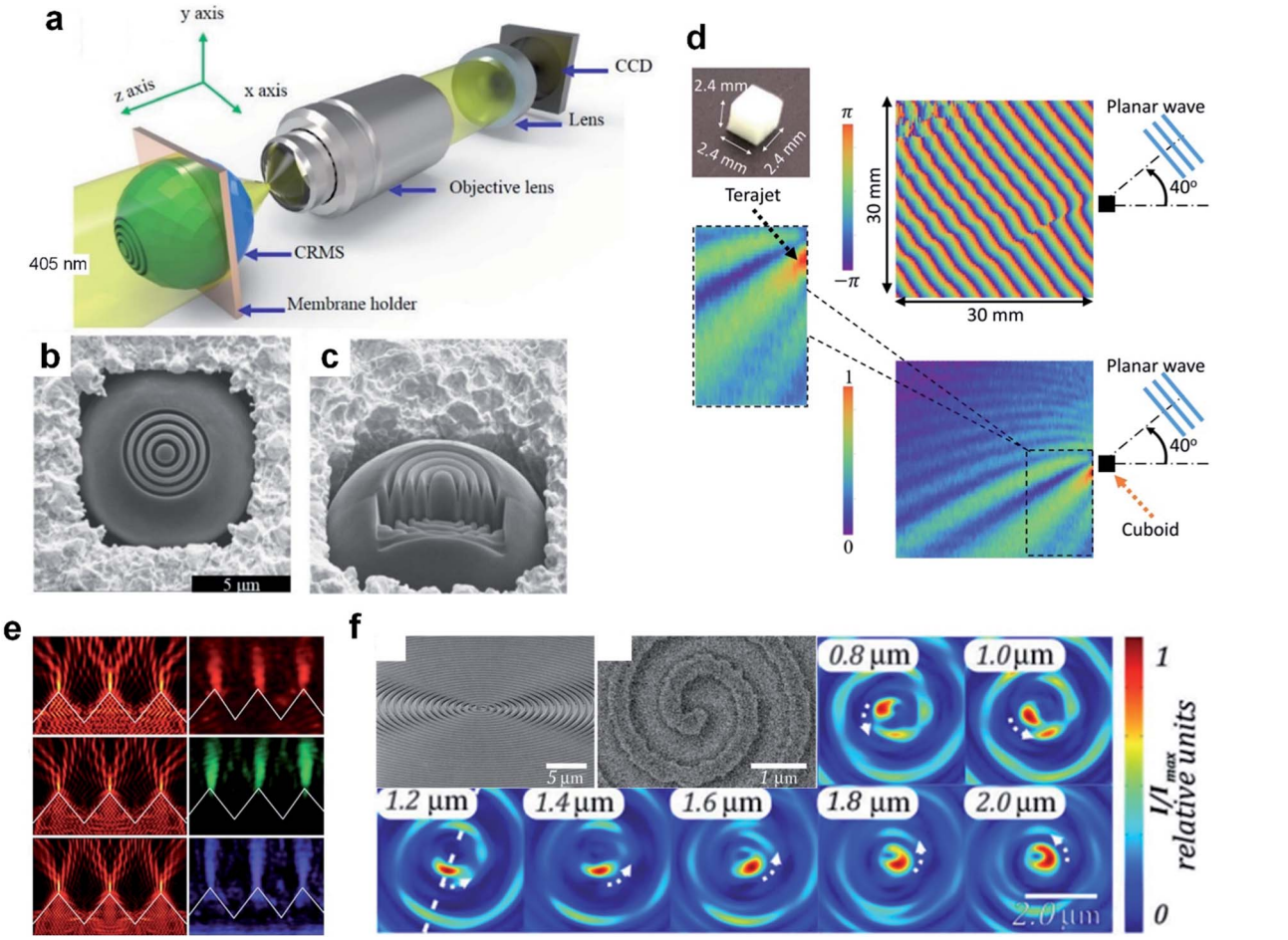

Fig. 4 (a) Schematic of measuring a PNJ by a conventional optical microscope. The lens located between the objective lens and the CCD is the focusing lens. (b) Top and (c) side views of a microsphere decorated with 4 rings. Reproduced with permission from ref. 101. Copyright 2015, Optical Society of America. (d) A fabricated polytetrafluoroethylene cube and the experimental visualization of the phase and amplitude profiles of the PNJ. Reproduced with permission from ref. 109. Copyright 2017, American Institute of Physics. (e) Experimental images (right) and FDTD simulation (left) of power flow distributions for the diffraction gratings at incident wavelengths of 671 nm, 532 nm, and 405 nm. Reproduced with permission from ref. 113. Copyright 2018, Institute of Physics. (f) Side view and top view SEM images of the central part of the manufactured spiral axicon, and intensity distribution in the cross-sections at different distances from the axicon surface. Reproduced with permission from ref. 114. Copyright 2016, Optical Society of America.

experimentally that Bessel-like PNJs can be obtained with properly engineered sub-wavelength core–shell colloids.[95] This form of geometry engineering is strongly inspired by a far-field approach for the generation of Bessel beams. Pacheco-Peña *et al.* demonstrated the ability of high-index dielectric hemispherical particles immersed in air to generate PNJs with extreme resolution ($\sim 0.06\lambda$).[96] Huang *et al.* employed a genetic algorithm coupled with Mie theory to optimize the magnetic field intensity distribution of PNJs generated by multilayer microcylinders at visible wavelengths in free space.[97] Zhou showed that a micro-gold tube illuminated by a TM-polarized plane wave could generate a stronger PNJ than that generated by dielectric cylinders with the same dimension.[98] Hengyu *et al.* reported that a PNJ with a small FWHM of 0.398λ ($\lambda = 0.4$ μm) can be achieved by illuminating the curved side of a hemispheric shell possessing a high refractive index and properly chosen diameters and thickness.[99] McCloskey *et al.* experimentally demonstrated that high intensity PNJs with nanoscale footprint and low divergence can be generated in a system of Si_3N_4 microdisks illuminated from the side with purple, green, and red laser light.[100] Wu *et al.* reported that the features of a PNJ can be changed by decorating the dielectric microsphere surface with concentric rings.[101] See the schematics of the decorated microspheres, the brightfield microscope, and fabricated samples shown in Fig. 4(a–c). They demonstrated that a FWHM waist of 0.485λ ($\lambda = 0.4$ μm) is achievable by engineering the microsphere with four rings etched to a depth of 1.2 μm and a width of 0.25 μm. Wu *et al.* further generalized the idea of decoration for microsphere surface by covering the center of a microsphere with a flat mask, to engineer PNJs.[102] These works have demonstrated that both global and local modification for microspheres or microcylinders can significantly affect the properties of the generated PNJs.

In fact, PNJs are not an exclusive feature of spherical objects, but many structures with aspherical edges have now been involved because of their capability in generating PNJs with distinct features. It has been shown experimentally that square-profile microsteps on a silica substrate, can produce sub-diffraction-limit PNJs with enhanced intensity near the surface *via* the illumination by a linearly polarized laser beam of wavelength $\lambda = 633$ nm.[103] This device is similar to the dielectric cuboids being tested in various illumination modes.[104–108] The dielectric cube can produce an asymmetric phase anomaly and Gouy phase shift at the terahertz frequency, which cannot be explained simply as an analogy to a lens focusing a Gaussian beam.[109] See the cube and experimental results in Fig. 4(d). Zhang *et al.* proposed a microtoroid structure with high index ($n = 3.5$) to generate an ultralong PNJ.[110] Geints *et al.* reported on the calculations of optical radiation scattering at micrometer-sized axicon particles and showed that PNJs with up to $\sim 25\lambda$ length are achievable without sacrificing high peak intensity and sub-wavelength transverse width.[111] We can, undoubtedly, assemble the aforementioned individual PNJ generators as a periodic grating [see one of the representative images shown in Fig. 4(e)], so that massive arrays of PNJs can be generated simultaneously for diverse applications like sub-diffraction imaging, interferometry, and surface fabrication.[34,112,113] Degtyarev *et al.* proposed an interesting extension for PNJs (*i.e.*, the generation of a PNJ with a helix shape), which is called photonic nanohelix.[114] See the image of the central part of the manufactured spiral axicon obtained with a scanning electron microscope (SEM) in Fig. 4(f). This potentially adds a new dimension to the optical manipulation of nanoscale objects based on PNJs. By analogy with the index engineering, one may expect a deformation-controllable dielectric geometrical profile to dynamically tune the parameters of PNJs. In fact, the controllable deformation of specific polymers and silicon nanostructures have already been realized *via* diverse approaches including light,[115] electricity,[116,117] gas,[118] and force.[119] These techniques, as an alternative to the engineering of refractive index, potentially pave the way to the controllable PNJs for diverse applications.

2.5 Non-conventional designs of PNJs

For the majority of PNJ generators, the excitations, *e.g.*, plane waves or Gaussian beams, are free-space propagating waves. Although propagating waves can generate the sub-diffraction-limit waist of some PNJs, excitation *via* non-conventional sources can produce interesting features of the localized field. Specifically, it has been reported that a PNJ can be excited by surface plasmon polaritons (SPPs) at the shadow-side surfaces of dielectric microdisks positioned on gold films.[120] The SPP-assisted PNJ can propagate over several optical wavelengths without sacrificing a subwavelength FWHM. The strong amplitude of the SPPs makes it possible to generate a PNJ with ultra-high field concentration, which shows great promise for enhanced Raman scattering and integrated plasmonic circuits. Similar investigation on SPP-assisted PNJs can be found for 3D dielectric cuboids[121] and a cube with a prism.[122] The SPP-assisted PNJ generation, theoretically, can be regarded as a phenomenon in two-dimensional systems because the SPPs are confined to the interface of a metal–dielectric composite. However, the short propagation length of SPPs in a planar system notoriously hinders the diverse applications of the proposal of a 2D PNJ. Recently, Kim *et al.* solved this problem and explored, numerically and experimentally, the use of Bloch surface waves sustained by a suitably structured dielectric media to enable subwavelength focusing in a planar optical system.[123] See Fig. 5(a–c). A similar investigation was also implemented by Kim for a two-dimensional fraxicon.[124] Augenstein *et al.* utilized the same experimental configuration as in Kim's work, to focus Bloch surface waves down to a sub-wavelength scale through a pixelized PNJ generator rather than triangles.[125] So far, the generation of PNJs is primarily achieved by focusing the central parts of excitation beams (either in 2D or 3D forms), but we should mention that the focusing properties are also governed by the edge diffraction, making it possible to observe tilted PNJs on the edge of a customized dielectric microstructure.[126] See the results for a customized microstructure shown in Fig. 5(d). Apparently, the introduction of non-conventional excitation modes adds another dimension to the tuning of PNJs, making it a promising ingredient for a future generation of integrated photonic devices or lab-on-chip devices for specific sensing applications.

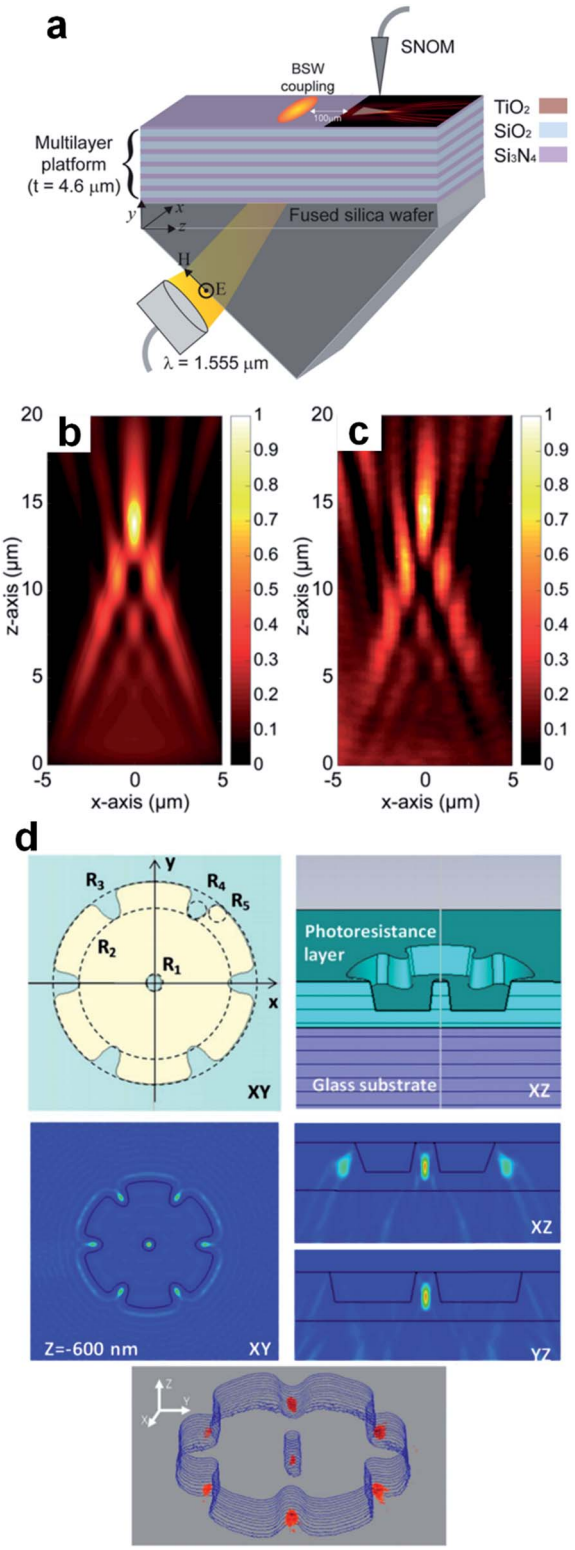

Fig. 5 (a) Schematic of the experimental setup including the multilayer structure, Kretschmann coupling configuration, and the scanning nearfield optical microscope probe. (b) Simulated result for the x–z intensity distribution. (c) Measured near-field intensity distribution of the fabricated funnel device. Reproduced with permission from ref. 123. Copyright 2017, American Chemical Society. (d) Near field focusing with a flower-shaped cavity. Reproduced with permission from ref. 126. Copyright 2018, Optical Society of America.

2.6 Generalized design framework for PNJs

The underlying physics of the generation of PNJs, essentially, is the diffraction and interference of light in the volume with dimensions comparable to or larger than the wavelength, which could happen in either the far-field or the near-field. Such an essence indicates that arbitrary-shaped microstructures, with wavelength-scale dimensions, may offer similar functionality as that of the aforementioned PNJ generators.[112] The PNJ generators (for instance, microspheres and their derivatives, cuboids, and axicons) as have been reviewed in Sections 2.2–2.4, can be regarded as being obtained from the basic shapes of nature and our physical intuition. However, those conventional shapes and their derivatives only occupy a very limited space of possible PNJ designs. For this reason, we review the generalized framework that could guide the design of PNJ generators with non-conventional shapes, and present preliminary results, to extend current researches and guide future efforts in the field of PNJ design.

The key to engineering PNJ generators for specific functionality, without any doubt, is inverse design. It is limiting to attempt to find optimal designs through physical intuition and through secondary developments based on the traditional templates of the standard photonic design library (*e.g.*, spheres, cuboids, and axicons). Hence, we need an inverse design framework that can explore a maximum number of degrees of freedom. For this reason, topology optimization (TO) may be the best choice, because TO is more general than shape optimization or sizing optimization in the sense that the design can attain any shape within the design space, instead of dealing with predefined configurations.[127–133] In fact, TO has been utilized extensively in the design of photonic devices, especially in the fields of photonic crystals, waveguides, and bandpass filters.[134–143] For the design of PNJs based on TO, the fundamental physics is that each dielectric optimization element (*e.g.*, a mesh element), whose size is much smaller than the excitation wavelength, behaves like an electric dipole with unique orientation, strength, and phase lag.[144–149] The coupling among all the optimization elements have a strong impact on each individual dipole, which can be approximately described *via* the semi-analytical theory of discrete dipole approximation.[150–158] It is the coupling among all the fundamental elements that enables us to control the microscale or macroscale performance of photonic devices by playing with the material layouts. Consider now a 2D box ($6\lambda \times 5\lambda$) with refractive index $n = 2$ surrounded by vacuum ($n = 1$); see Fig. 6(a). Our goal is to concentrate the energy of a 633 nm plane wave that illuminates the bottom side of box, to a region with footprint $1\lambda \times 1.5\lambda$ at a fixed distance of 7λ above the box. Without any optimization, the field distribution is primarily dominated by the edge scattering of the box, and no energy concentration is observed [see Fig. 6(a)]. To optimize the box with TO, we can formulate the optimization problem in the form as:

$$\begin{aligned} \underset{\rho}{\text{maximize}} \quad & F = \int_{\Theta} |E(\rho)|^2 \mathrm{d}s, \rho \in \Omega \\ \text{subject to} \quad & G_0(\rho) = \int_{\Omega} \rho \mathrm{d}s - S_0 \leq 0. \end{aligned} \tag{4}$$

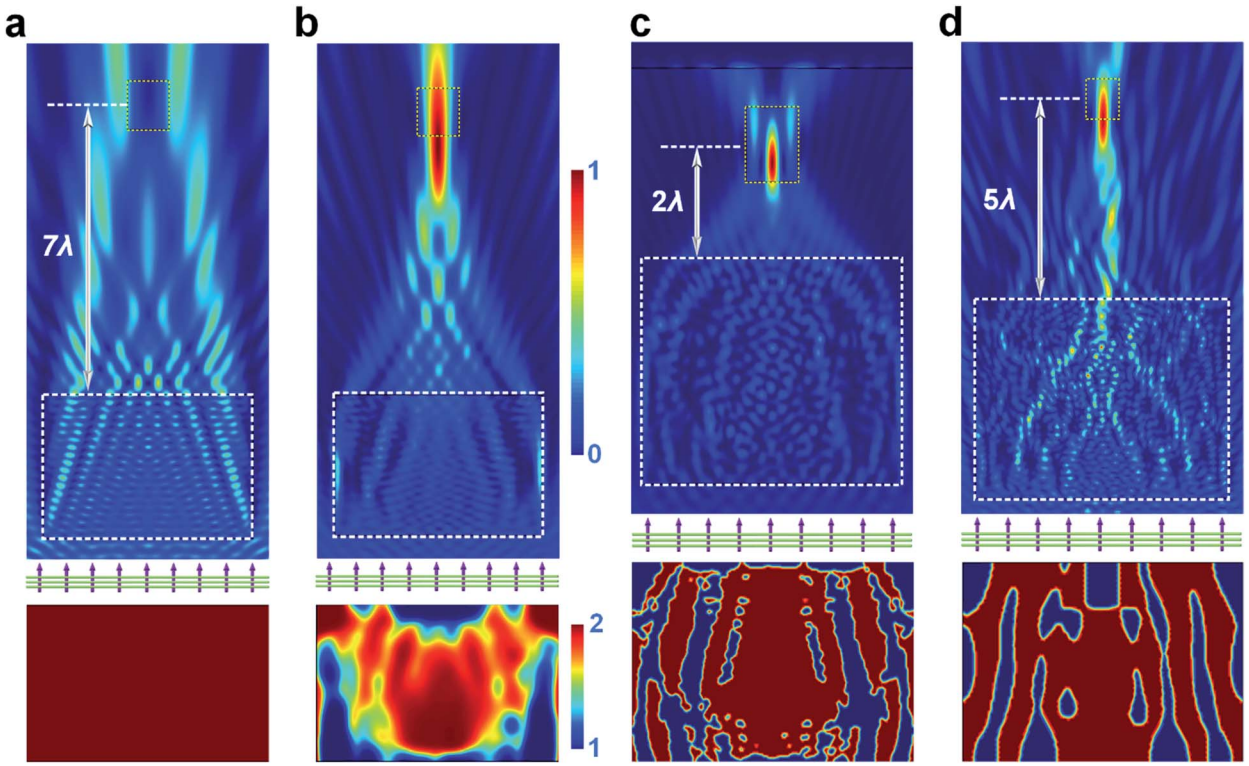

Fig. 6 (a) Scattering by a 2D cuboid without optimization. (b) An elongated PNJ generated by a material layout with index spanning the entire range 1–2. Tight PNJs with (c) short and (d) long focal lengths as generated by binary material layouts with different features.

where F is the objective function representing that the energy stored in the region Θ, with footprint $1\lambda \times 1.5\lambda$ at a fixed distance of 7λ, should be maximized. E represents the electric field in region Θ as a function of the density ρ in the optimized box. ρ can be either 1 or 0, representing if the material $(n = 2)$ is present or not. S_0 is a pre-defined constant for the constraint G_0 that ensures that the volume occupied by the material $(n = 2)$ cannot exceed S_0.

In the density-based TO approach, the design region is meshed and a discretized density variable ρ_i is assigned on every mesh element (or other fundamental unit). The refractive index at element i in the box is typically calculated using:

$$n_i = \sqrt{\varepsilon_1 + \rho_i(\varepsilon_2 - \varepsilon_1)}, \tag{5}$$

where ε_1 and ε_2 are the permittivities of vacuum and the material, respectively. The globally convergent method of moving asymptotes, whose code was provided by Prof. Svanberg, is used for solving the optimization problem eqn (4).[159] ρ_i must lie between 0 and 1 to facilitate the gradient-based method of moving asymptotes. In every iteration, the value of ρ_i is filtered by smoothing the values using a standard density filter. This filter modifies the element density to be a function of the densities in a specified neighborhood of an element (characterized by the radius R),[160]

$$\rho_i^{\text{filt}} = \frac{\sum_{j \in N_i} \rho_j v_j w_{ij}}{\sum_{j \in N_i} v_j w_{ij}}, \tag{6}$$

where v_j is the volume of the j^{th} element. Because a fixed pixel is used on which each density variable is assigned, v_j is a constant given by the product of the length and width of the pixel. w_{ij} is the weight factor assigned based on the distance of the neighbouring pixel from the i^{th} pixel, given by

$$w_{ij} = \max\left(R - |\vec{r}_i - \vec{r}_j|, 0\right), \tag{7}$$

where $\vec{r}_i$ and $\vec{r}_j$ are the coordinates of the i^{th} and j^{th} pixels respectively. We should mention that R is a variable specified by users to control the smallest feature size in the optimization, *i.e.*, smaller R generally results in smaller feature sizes in the final material layout. The standard density filter shown in eqn (6) does not prevent grayscale (*i.e.*, intermediate densities). Even with penalization schemes, grayscale features are introduced in a transition region between the different materials. The standard density filter acts as a base upon which other filters are built (*e.g.*, projection filters). Several filters based on Heaviside projections have been proposed in the literature in order to achieve discrete designs and minimum length scales on one or all materials.[161] Here, we use a modified form of the approximated Heaviside function projection to process the density variable. The approximated Heaviside function is given as[162]

$$\tilde{\rho}_i\left(\rho_i^{\text{filt}}, \beta, \eta\right) = \frac{\tanh(\beta\eta) + \tanh\left[\beta\left(\rho_i^{\text{filt}} - \eta\right)\right]}{\tanh(\beta\eta) + \tanh[\beta(1-\eta)]}. \tag{8}$$

Here, the value of η is chosen by a Golden Section Search Algorithm. The value of β is used to control how well the Heaviside function is approximated. If the objective function's

change after an iteration is smaller than a threshold value, the value of β is increased by a factor of 2. Note that $\tilde{\rho}_i$ is the final density variable used in the optimization eqn (4).

We now implement the optimization to design a PNJ generator with tight FWHM and elongated length. The bottom of Fig. 6(b) shows an intermediate material layout before the final binary output. In the top of Fig. 6(b), we can clearly find an elongated PNJ generated on the back side of the optimized box. The material (refractive index) distribution in the box is not binary but rather spans the entire range 1–2. As the optimization begins to converge to the maximum of the objection function F, β increases constantly so that the final output of the optimization goes towards a binary layout.

Next, we optimize the design to focus at different distances from the lens. Fig. 6(c) presents an optimized result that behaves like a nearfield lens with a short focal length around 2λ. The controlling variable R is preset as 0.15λ, indicating many small features in the optimized box. See the binary material layout at the bottom of Fig. 6(c). To make the design compatible with state-of-the-art top-down fabrication techniques, we can enlarge R so that small features can be avoided in the final output. Fig. 6(d) presents another design of a lens with a relatively large focal length around (5λ) that corresponds to $R = 1.1\lambda$. By comparing with the one shown in Fig. 6(c), we can clearly observe that the material layout in Fig. 6(d) has much larger features and the material distribution is much more uniform, making the real fabrication of the planar devices more feasible. A large R results in a fabricable device, but it sacrifices many degrees of freedom during optimization. Therefore, one has to make a trade-off for the specific application.

To further improve the fabricability, a specific case of TO has been developed by using fundamental geometries like cylinders and cuboids,[163] rather than the mesh elements, as the building blocks to design photonic devices.[164] Selecting the fundamental unit to be a cuboidal voxel whose size is independent of the mesh is preferable because the mesh can be refined as needed for accurate simulation without affecting the size of the features generated and thus the manufacturability. As one of the demonstrations, Augenstein *et al.* utilize the cuboid-based inverse photonic design strategy to attain functional elements that focus Bloch surface waves efficiently into spatial domains slightly smaller than half the wavelength.[125] They validated the devices by measuring the field distributions with a scanning near-field optical microscope. See Fig. 7(a and b) for the schematic and simulated PNJs. These specific cases of TO are seamlessly compatible with top-down fabrication techniques like dry-etching and FIB, and they enable the design of PNJs with specific performance features (including focal length, working distance, NA, sub-diffraction FWHM, and field enhancement) that cannot be achieved by conventional PNJ generators as aforementioned; thus, we anticipate, TO will be applied extensively in the area of PNJ in the near future.

We should emphasize at the end of this section that each of the aforementioned PNJ engineering techniques (including index engineering, geometry engineering, non-conventional designs of PNJs, and the generalized design framework for PNJs) enable the customization of all the features of PNJs such as the FWHM, working distance, concentration of electromagnetic energy, and gradient fields. Therefore, they are the basis to the diverse applications of PNJs because a specific application of PNJ is built upon one or several features of PNJs. For this reason, we categorize the diverse applications in the following section according to the application of specific features of PNJs.

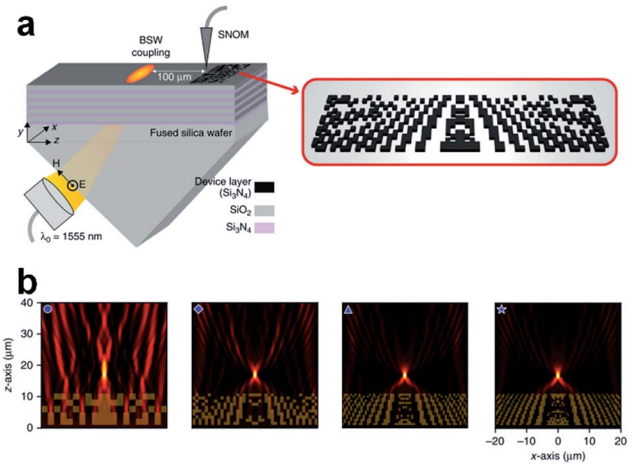

Fig. 7 (a) Schematic of the experimental scheme (left) and a representative pattern of a relevant functional element (right). (b) Optimization of different structures that can focus Bloch surface waves behind the functional element. The optimized structures are shown in yellow. Reproduced with permission from ref. 125. Copyright 2018, Nature Publishing Group.

3. Diversity in the applications of PNJs

PNJs have many extraordinary properties such as deep-subwavelength FWHM, hot spot with intensive electromagnetic energy, gradient field distribution, backscattering enhancement, and microlensing and resonance effects. The aforementioned PNJ engineering techniques pave the way to customize these features of PNJs and thus may catalyze diverse applications. In the past decade, we have witnessed a bloom in the application of PNJs in many fields spanning from super-resolution imaging and nanoscale sensing to fluorescence enhancement and optical manipulation. We therefore try our best to give a comprehensive review on the emerging fields by categorizing them in terms of the aforementioned properties of PNJs. Among all the applications, it is not surprising that the ones utilizing the feature of high-energy concentration of PNJs dominates, because the high energy-to-volume ratio is the most straightforward advantage of dielectric PNJ generators (especially microspheres). The highly concentrated electromagnetic energy may even trigger the nonlinear effect in materials and thus expands the territory of PNJs to the more universal light–matter interactions for enhancing the existing nonlinear photonic devices. The other properties of PNJs such as gradient field distribution and microlensing effect may facilitate the creation of novel photonic devices such as biophotonic waveguides and spherical photonic crystals. We believe that PNJs will demonstrate their value in more and more exciting fields.

3.1 Deep-subwavelength FWHM and nearfield effect of PNJs

It has been extensively reported that PNJs generated by dielectric microspheres can be subdiffraction-limited. A very recent study even showed that the FWHM through material engineering methods can reach $\lambda/7.3$.[165] This opens new possibilities in a variety of research areas. Moreover, if the narrow PNJ generated by a PNJ generator (for instance, microspheres) is in close contact with a sample surface, a local field enhancement in the area between the bottom of the generator and the sample surface may be established, making the light-matter-interaction occur in an unconventional manner. Super-resolution imaging, nanofabrication beyond diffraction limit, and high-density optical data storage are representative examples that to some extent benefit from the subdiffraction-limited waist of PNJs and nearfield effect.[166]

Super-resolution imaging. Using microsphere-generated PNJs for imaging is probably the most direct application because the light focusing properties of the microsphere are analogous to those of a macroscale optical lens. However, the imaging resolution beyond the Rayleigh limit *via* the contacted "microsphere lens," makes the PNJ-assisted imaging significantly different to any known conventional far-field-based imaging modalities.[51,167,168] Specifically, it has been reported that a solid immersed lens (nanolens) with $n = 1.5$ can resolve features beyond the diffraction limit.[169] These nanolenses, in contrast to geometrical optics lenses, exhibit curvilinear trajectories of light, resulting in remarkably short near-field focal lengths. Although the terminology PNJ was not emphasized in this work, the capability of focusing incoming waves in the nearfield region of the nanolens was appreciated. Wang *et al.* used dielectric microspheres (with $n < 2$) rather than solid immersed lenses, to achieve optical imaging at 50 nm lateral resolution using white-light illumination.[26] More discussions on the imaging modes, magnification, as well as the size and index dependence can be found in the review article ref. 21. A standard configuration of the microsphere-based super-resolution imaging and several representative super-resolution images (including those from both microspheres and solid immersion lenses) are shown in Fig. 8(a–c). The field of microsphere nanoscopy has grown and extended rapidly in terms of applications, nearfield lens design, and theory development,[170] since the works by Lee and Wang. Li *et al.* described white-light optical imaging of 75 nm adenoviruses by submerged microsphere optical nanoscopy without the use of fluorescent labeling.[171] Krivitsky *et al.* presented a method of positioning and controllable movement of a microsphere by using a fine glass micropipette.[172] Darafsheh *et al.* demonstrated a series of advantages of microsphere-assisted imaging over confocal and solid immersion lens microscopies including intrinsic flexibility, better resolution, higher magnification, and longer working distances.[173,174] Yang *et al.* used high-refractive

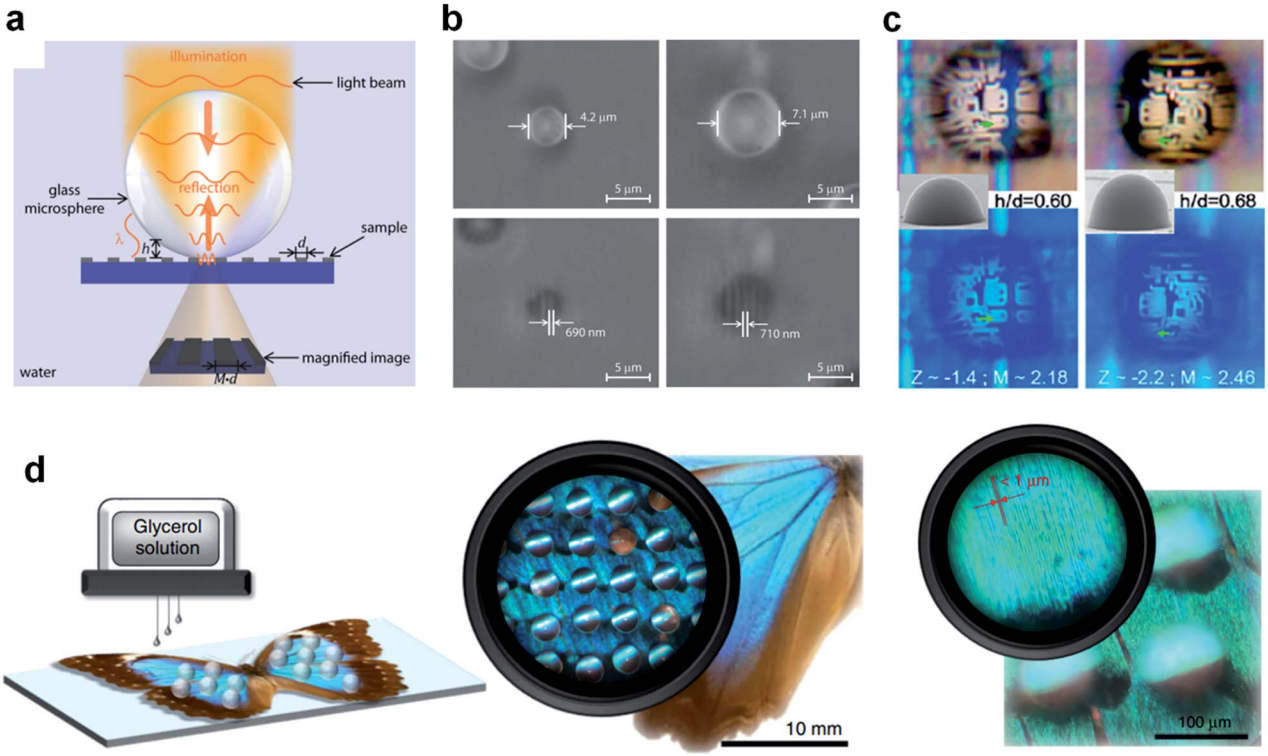

Fig. 8 (a) Schematic of the microsphere-based super-resolution imaging process. (b) Optical microscope images of the nanolenses on patterned substrates. Reproduced with permission from ref. 31. Copyright 2016, American Chemical Society. (c) Super-resolution imaging for microelectronics using hSILs with various lens curvatures. Reproduced with permission from ref. 176. Copyright 2016, American Chemical Society. (d) *In situ* printing of glycerol superlenses for the super-resolution imaging of nanostructures on butterfly wings. Reproduced with permission from ref. 179. Copyright 2019, Nature Publishing Group.

index ($n = 1.92$) glass microspheres for facile and affordable super-resolution fluorescent imaging of sub-cellular organelles and biomolecules.[175] Zhu *et al.* synthesized ZrO_2/polymer hybrid colloidal microspheres as high-index hybrid solid immersion lens to achieve super-resolution imaging of 45 nm under a standard white light or blue light optical microscope.[176] Hao *et al.* reported optical nanoscopes based on partially-immersed microspheres and a microfiber (as an evanescent illuminator), respectively.[177,178] To enable the microsphere-based super-resolution imaging for many applications, an *in situ* printing technology has been developed to print liquid superlenses on top of nanostructures for dynamically colorful super-resolution imaging.[179] See the schematic diagram and the magnified image in Fig. 8(d). More systematic studies as well as the applications of microsphere-based (or the derivatives of microspheres such as liquid droplets and microfibers) imaging can be found extensively in the mainstream optics and photonics journals.[48,180–188]

Different than other super-resolution imaging techniques like hyperlens and superlens,[189–191] super-oscillation lens,[17,192–194] and fluorescence-based modalities,[195,196] the underlying physics of imaging beyond the Rayleigh limit *via* dielectric microspheres has not been completely revealed yet, although there was a study that claimed that it is due to the FWHM of PNJs.[31] Maslov *et al.* investigated the theoretical limits of resolution available in microsphere-based nanoscopy using incoherent point emitters in the air.[197] Zhou *et al.* investigated the effects of immersion depth on super-resolution properties of microsphere-assisted nanoimaging with different indices.[198] Li *et al.* investigated the unusual imaging properties of super-resolution microspheres by comparing their results with the output of many proposed theories.[199] Yang *et al.* experimentally validated that shrinking the waist of the PNJ of a dielectric microsphere results in higher lateral resolution.[31] Duan *et al.* theoretically modelled the imaging process through a microlens with vectorial electromagnetic analysis, and then excluded the previously plausible explanation of super-resolution based on the super-focusing effect.[200] All the preliminary results show that, the sub-100 nm imaging resolution achieved by a microsphere with a perfect spherical shape need more physical investigation. In fact, the contact imaging mode in microsphere-assisted nanoscopy facilitates the interaction between microspheres and the evanescent components of the excited objects. The tunneling of evanescent waves into propagating waves and the transmission enhancement in the conversion,[27] akin to the scanning nearfield optical microscopes,[201] may be a potential direction for further investigations on the underlying physics of microsphere nanoscopy.

Nanofabrication. The diffraction limit is a fundamental barrier to the optics-based surface patterning technologies, such as optical lithography and laser direct writing.[202,203] Different from macroscale objective lenses in which the focused spot is diffraction limited, the PNJs generated by microspheres can be designed to have a beam waist that is much smaller than the diffraction limit. This makes it possible to pattern deep subwavelength structures in a form similar to direct laser writing but with much smaller features that are comparable to that of plasmon-assisted lithography.[204,205] In fact, when a microsphere is in close contact with a sample surface, a local field enhancement in the area between the bottom of the microsphere and the sample surface is established, making it easy to ablate the materials around the contact area.[170] Because of the spherical shape, early studies on microsphere-based laser direct writing were implemented "randomly," *i.e.*, microspheres were randomly distributed on the wafer surface before being illuminated by a laser.[206] After the exposure, the microspheres were washed away by deionized water combined with ultrasonic vibration.[207] Munzer *et al.* used isolated polystyrene spheres with diameters on the order of the laser wavelength to pattern holes on a silicon surface and on a glass surface.[208] For different materials, the local field enhancement behaves differently in terms of the concentrated energy and surface modes.[209] For the case of dielectric microspheres positioned on dielectric surfaces, the localized magnetic field enhancement usually accompanies the generation of electric field hot spots, making it possible to pattern invisible structures inside magnetic materials. For the case of a dielectric microsphere positioned on a metal surface, nearfield optical resonance effect may be excited at the dielectric–metal interface,[210] thus providing a stronger field enhancement.[211] But we should mention that the higher concentrated energy may not necessarily guarantee a better patterning effect because material properties (*e.g.*, melting point and rigidity) are also important.[212] The phenomena buried inside the sphere-substrate gap can be understood from the viewpoint of a nearfield lens and resonator mirror of a spherical cavity.[213] It is such a cavity effect that produces the localized field enhancement. It is not difficult to imagine that the cavity effect degrades significantly as the gap between the bottom of microsphere and sample surface increases. This explains why microsphere-based nano-patterning is operated in contact mode in most instances.[214]

It is apparent that the random distribution of microspheres prohibits the controllable fabrication of desired structures. Diverse methods, including self-assembly,[215–217] off-axis irradiation,[218] tweezing (either optical or mechanical),[219] and microlens arrays,[220] have been developed, to manipulate individual microspheres or microsphere arrays for fabricating customized patterns. The 3D coherent nanolithography process that utilizes the focal spots generated by a self-assembled periodic nanosphere array has been successfully developed in recent years. The Talbot field then exposes a pattern onto the underlying photoresist, recording the 3D intensity distribution. Nanostructures with feature size down to one-fourth of the operating wavelength were achieved.[221] See the schematic of the principle and experimental results in Fig. 9(a). A natural extension is that arbitrary periodic nanostructures with optimized topography can be utilized to create 3D patterns in photoresists.[222–226] Although the self-assembly method makes it possible to pattern over a large area, it is primarily used to fabricate nanoholes. Off-axis irradiation can be combined with the self-assembly method to fabricate arbitrary structure patterns.[170] The key for the off-axis irradiation method is varying both the illumination intensity and the illumination angle of the beam impinging on the microspheres such that both the strength and the position of

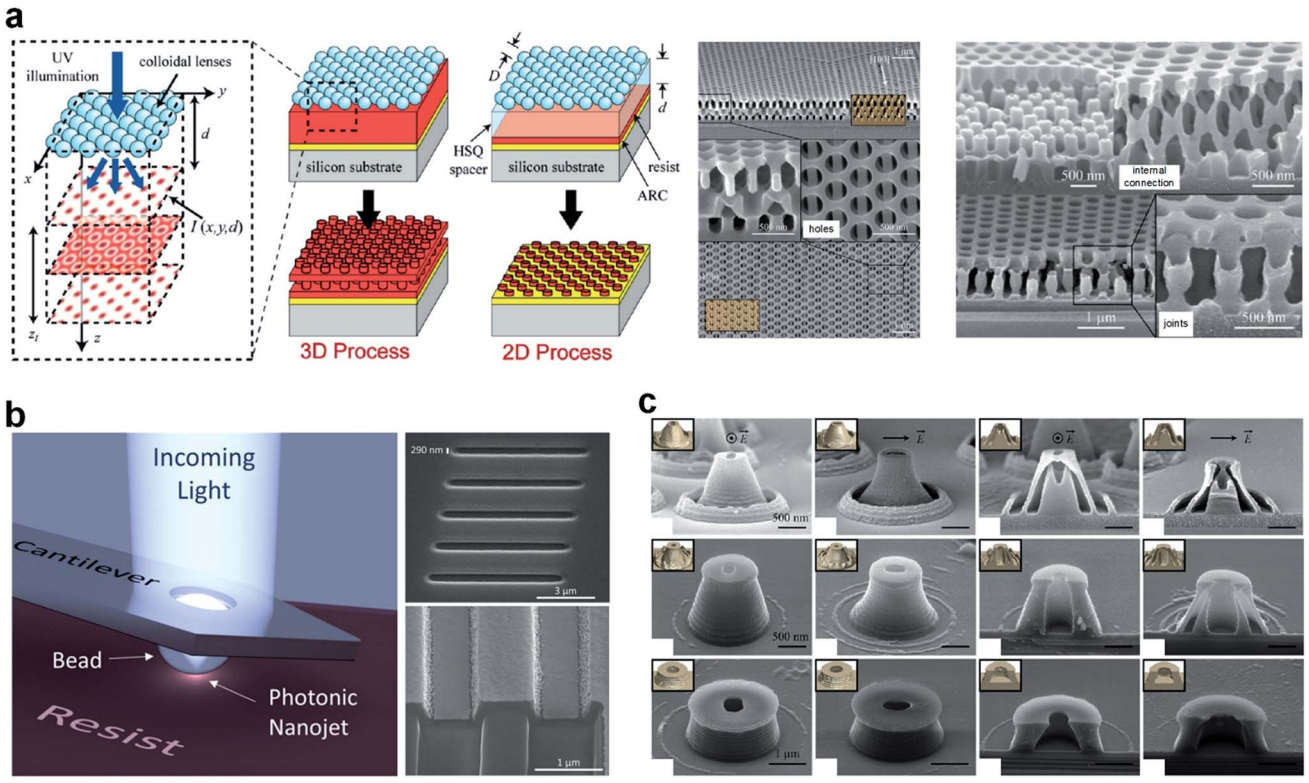

Fig. 9 (a) Schematic of PNJ-assisted 3D nanofabrication using nanospheres. A hexagonal array of nanospheres is illuminated by a UV laser to generate a 3D intensity distribution. The experimental results on the left side are the micrographs obtained for different layers. Reproduced with permission from ref. 221. Copyright 2011, American Chemical Society. (b) Schematic illustration and SEM image of a cantilever with a bead placed inside the circular rim. The right SEM images are the fabricated 2D nanostructures. Reproduced with permission from ref. 229. Copyright 2017, American Chemical Society. (c) Fabricated hollow 3D nanostructures using TE- and TM-polarized illuminations. Reproduced with permission from ref. 231. Copyright 2013, American Chemical Society.

the PNJs generated on the back side can be tuned. Li *et al.* used a self-assembled particle lens array with near-field enhancement effect to write millions of nano-sized user-defined features through off-axis irradiation.[218] They demonstrated that about a 5 mm × 5 mm area can be written with a single shot of a laser beam or a few scans for up to 100 million identical features of nano or sub-micro scales. Compared to the off-axis irradiation and self-assembly based nanopatterning, the utilization of either optical tweezers or mechanical cantilevers to hold microspheres can facilitate the fabrication of more uniform nanostructures.[227] This is especially the case when the microsphere is embedded in an atomic force microscopy (AFM) cantilever because the precise control of the AFM cantilever translates into precise positioning and movement of the generated PNJs.[228,229] See the cantilever-based nanolithography in Fig. 9(b). To further improve the throughput without sacrificing the positioning accuracy and pattern uniformity, one can embed multiple microspheres into a controllable stage so that it behaves like a microlens array. By properly choosing the illumination wavelength and the size of microspheres, the properties of PNJs can be customized to rapidly pattern superficial and 3D structure arrays.[230] A more easy-to-implement method to achieve controllable nanofabrication is varying the properties of illumination sources. This is because the properties of PNJs are sensitive to the illumination conditions [*e.g.*, polarization, phase (if multi-beam illumination is introduced), and angles]. See Fig. 9(c) showing the fabricated nanostructures as functions of polarization states.[231,232] We recommend ref. 228 to our readers for more information regarding microsphere-based nanofabrication.

Optical data storage. Optical storage, which is a method that uses a laser to store and retrieve data from optical media (such as a compact disc or a digital versatile disc), has driven modern society forward because of the ubiquitous need to save and access data. In optical storage, data is usually recorded by making marks in a pattern and read back using a focused laser that scans over the surface of the pattern.[233–235] The storage capacity, as can be imagined, depends significantly on the size of the probe beam. PNJs generated by dielectric microspheres have been demonstrated that can reach the size scale of $\lambda/5$ and even beyond, which is well suited for PNJ-based optical storage. Back in 2008, Kong *et al.* numerically investigated the possibility of using microspheres as the probe in an optical data-storage system.[236] They showed that PNJ-illuminated pits having 50 nm × 80 nm lateral dimensions yield a contrast ratio 27 dB greater than previously reported using a lens system for pits of a similar area. Similar works were also reported by investigating the detection of pits with lateral dimensions of 100 × 150 nm^2, and a 40 dB contrast ratio was observed. However, we should mention, the deep-subwavelength PNJ is achievable only at the

region very close to the back side of microspheres because of the requirement of the tailoring of evanescent-wave components. This indicates that the high-density PNJ-based optical storage scheme requires a working distance smaller than 200 nm for visible light illumination. Thus, a feedback mechanism with performance similar to that of the force-measurement in an AFM cantilever may be necessary. As 3D optical data storage arises, the PNJ-based high-density scheme faces challenges because the data stored in the pattern needs to be read in an entire volume rather than only on a surface. One solution is to design an ultra-elongated PNJ *via* the customization of either index or shape to facilitate depth scanning in the 3D disc, but with the sacrifice of resolution and thus storage density. The concept of the superoscillation lens, which can achieve deep sub-wavelength foci in the far-field domain,[192,237,238] offers a potential way to perform 3D optical data storage by combing the inverse design approaches and the concept of PNJs, but we should always keep in mind the trade-off between sidelobes and the strength of foci.[19,239] This is an open question that needs more investigations in the future.

3.2 Concentration of electromagnetic energy

From angular spectrum theory, the generation of PNJs indicates that there is wavefront modulation and constructive interference of different angular components. If the phase of most components are properly tailored, constructive interference can be maximized, leading to a hot spot with intense electromagnetic energy density. Such a high-energy PNJ can significantly enhance the performance of many existing devices and even trigger nonlinear effect in materials. A dielectric microsphere, which has a very high energy-collection-to-volume ratio, is a nearly ideal PNJ generator that has been used extensively in fields such as enhanced Raman scattering, enhanced second harmonic generation from monolayer materials, and optical surgery. Therefore, we will give a review for the emerging fields that are primarily built upon the high-energy concentration feature of PNJs.

Fluorescence enhancement. Strategies for controlling and enhancing the fluorescence of molecules and nanocrystals have been the subject of intense research in the past few decades. This trend is motivated by the need to develop new highly sensitive bio-sensors and by the possibility to improve opto-electronic devices like light emitting diodes and solar cells. PNJs generated by dielectric nanostructures can enhance the absorption of materials and change the excitation rate of molecules, without suffering the drawbacks of metallic nanostructures such as high absorption loss and heat generation.[240,241] Relying on this, a near-field optical study of TiO_2 nanodisks by fluorescence scanning near-field optical microscopy has been implemented recently. The localization of light and the fluorescence enhancement near the dielectric structures were visualized with a lateral resolution of $\lambda/5$ using an Er/Yb-codoped fluorescent nanocrystal glued at the end of a sharp scanning tip. It was demonstrated that the intensity patterns strongly depend on the disk size, forming lobes for a diameter close to the wavelength and a single bright spot for smaller structures. Although the experiments were performed off resonance, a maximum fluorescence enhancement of 2.3 was observed near 700 nm-wide disks [see Fig. 10(a)].[242] Vasista *et al.* studied the molecular fluorescence emission mediated *via* whispering gallery modes (WGM) of microspheres [see Fig. 10(b)].[243] Their experiments of this study reveal intensity dependence of split modes of the cavity as a function of in-plane wavevector and emission polarization in the far field. Such a mechanism, as has been demonstrated *via* photoemission electron microscopy,[244] facilitates enhanced fluorescence correlation spectroscopy. In this method, an optical fiber combined with a latex microsphere achieved single molecule level sensitivity because of PNJ effects.[245] Another exciting application of microbeads is upconversion fluorescence amplification. Conventionally, upconversion luminescence intensification requires controls over several factors such as composition and size of nanophosphors. The superlensing effect generated by dielectric beads provides an unprecedented and direct method to amplify the luminescence [see Fig. 10(c) showing the schematic illustration of an experimental setup].[246] Analogously, it has been demonstrated that a living yeast or human cell can also behave as a bio-microlens to enhance the upconversion fluorescence by 2 orders of magnitude. Because the focusing effect of a microbead relies heavily on the wavefront of excitation field, we anticipate that wavefront engineering may further enhance the upconversion fluorescence. Here, we should mention, the fluorescence enhancement is dominated by the electric field effect, while the symbiotic concentration of magnetic field in the PNJs, has rarely been investigated. The simultaneous generation of magnetic and electric spots is an extraordinary property of dielectric nanostructures,[247] making PNJ generators an ideal candidate for investigating magnetics-related phenomena.

Enhanced Raman scattering. To overcome the limited Raman signals due to the insufficient Raman scattering cross-section in a low-concentration environment, various strategies have been proposed. They can be mainly categorized into two mechanisms, *i.e.*, chemical enhancement and electromagnetic enhancement.[248] Compared to chemical enhancement, electromagnetic enhancement typically offers a much higher enhancement factor. This electromagnetic enhancement is conventionally attributed to localized surface plasmon resonances (LSPRs) generated by metallic nanostructures. However, in LSPR-based surface-enhance Raman scattering (SERS) schemes, severe loss due to interband transitions leads to Joule heating of the structure and the surrounding environment, which may cause damage to analyte molecules, and hence is not desirable in practical applications.[249] Dielectric systems are characterized by a much greater variety of parameters and properties that can be tailored to achieve enhanced Raman scattering or related effects. Light-trapping and subwavelength-focusing capabilities, morphology-dependent resonances, control of band gap and stoichiometry, and size-dependent excitons are a few examples.[13,249]

Dielectric microspheres have enhanced the Raman scattering signal by up to 10^{20} or more in perfectly smooth spherical resonators using WGMs.[250] It is known that evanescent waves

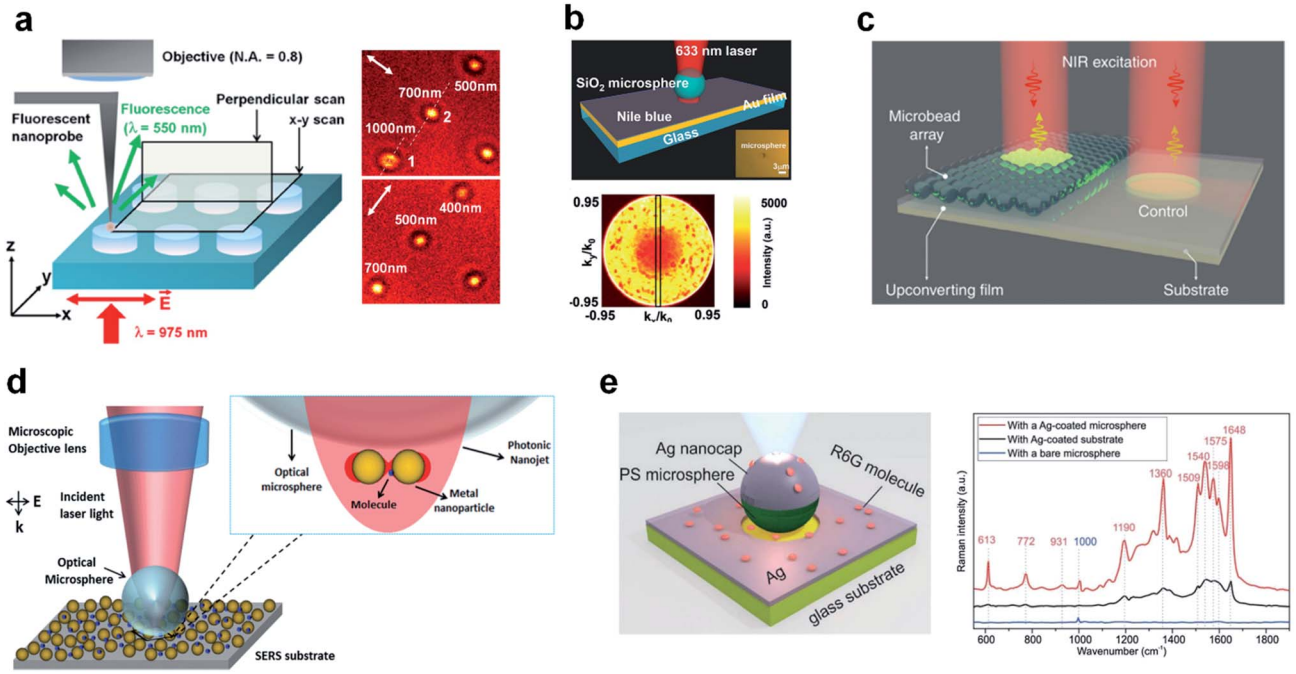

Fig. 10 (a) Schematic diagram showing the illumination configuration of the fluorescence scanning near-field optical microscopy, and representative experimental results. Reproduced with permission from ref. 242. Copyright 2017, American Institute of Physics. (b) Schematic of a system consisting of a metal film coupled to a SiO_2 micro-resonator, and the Fourier space image captured from a microsphere that is coupled to a Nile blue coated glass substrate. Reproduced with permission from ref. 243. Copyright 2018, John Wiley & Sons, Inc. (c) Schematic illustration of an experimental setup designed for luminescence amplification. Reproduced with permission from ref. 246. Copyright 2019, Nature Publishing Group. (d) Schematic of the PNJ-based Raman scattering enhancement mechanism, and an optical image showing a microsphere excited by a laser. Reproduced with permission from ref. 252. Copyright 2016, American Institute of Physics. (e) Schematic showing enhanced Raman scattering using an Ag-coated dielectric microsphere scheme, and the measured Raman spectra for R6G on an Ag-coated glass substrate. Reproduced with permission from ref. 259. Copyright 2019, John Wiley & Sons, Inc.

that propagate tangent to the sphere's surface and can extend outward for several hundreds of nanometers.[251] Thus, any molecule adsorbed onto the sphere's surface can be interrogated many times by the circulating photons;[252,253] thus, microspheres with sizes of $r \gg \lambda$ are potentially powerful tools for the label-free sensing of surface analytes.[254] However, the resonance feature of microspheres is not the only mechanism for Raman scattering enhancement. PNJs induced by microspheres with sizes in the range of 2–40λ can achieve similar results because the light in the PNJ can be concentrated into a volume that is one order of magnitude smaller than that for conventional focusing lenses. Yi *et al.* used a narrow PNJ (*i.e.*, a waist of 120 nm and a height of 100 nm) to enhance the Raman peaks of silicon.[255] Alessandri *et al.* utilized similar SiO_2 microspheres as versatile, universal Raman scattering enhancers. They demonstrated that the detection limits can be improved by several orders of magnitude, for different substrates consisting of diverse materials.[256] The PNJ-based Raman scattering enhancement, generally, can be illustrated by a laser-excited microsphere positioned in an environment of surface analytes.[257] See the schematic and a laser-excited microsphere in Fig. 10(d).[258] This can be regarded as the foundation of other PNJ-based Raman scattering enhancement mechanisms. For instance, the Raman signal from metal-coated dielectric microspheres interacting with 10^{-6} M Rhodamine 6G molecules, as measured on the microsphere's top surface, is up to seven times larger than that measured from a flat silver film. An enhancement factor of up to 10^8 is estimated compared with the case of a non-plasmonic microsphere surface. See the schematic and the measured Raman signal for R6G in Fig. 10(e).[259] The combination of metal and dielectrics, as well as doped semiconductors (so that Joule heating can be controlled without sacrificing the dielectric properties), opens up new possibilities for the PNJ-based Raman scattering enhancement.

All-optical switching. An all-optical switch is a device that allows one optical signal to control another optical signal, *i.e.*, control of light by light. All-optical switching must be implemented with consideration to demands for low switching energies and ultrafast switching times.[260] A PNJ-based focal geometry that can concentrate weak light energy into a deep-subwavelength volume is an ideal candidate for low-energy optical switching. Born *et al.* utilized a dielectric microsphere to form a high-intensity PNJ in a semiconductor nanoparticle material system. Femtojoule switching energies and femtosecond switching times have been observed in all-optical switching experiments.[261] The pump–probe experimental setup, in which the GaAs and Si targets use pump and probe pulses with respective wavelengths of 780 and 1550 nm, is shown in Fig. 11(a). Experiments with microspheres coated by

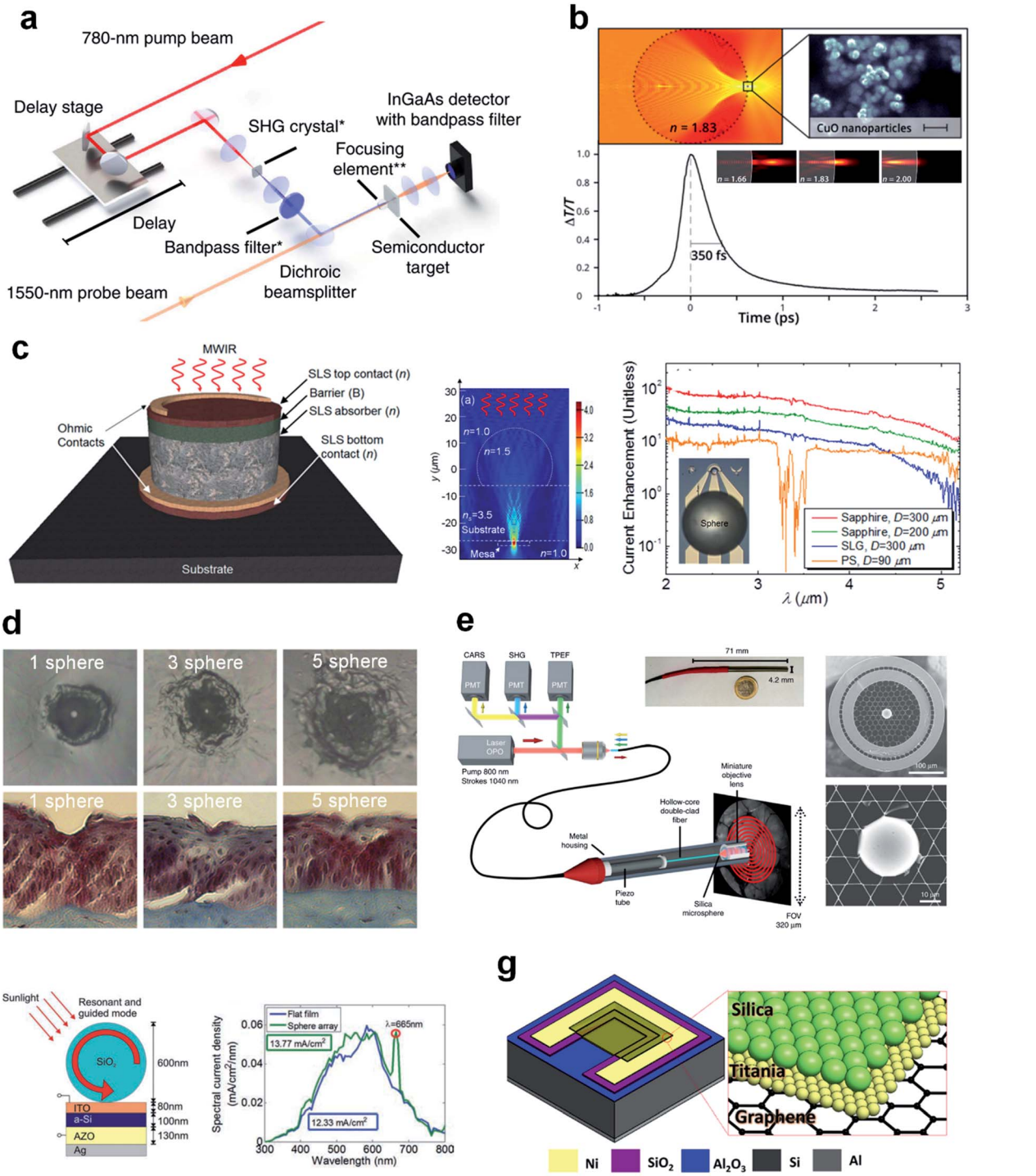

Fig. 11 (a) Schematic of the pump–probe experimental set-up. A 780 nm pump beam is used for the GaAs and Si targets and a 390 nm pump beam is used for the SiC target. Reproduced with permission from ref. 261. Copyright 2015, Nature Publishing Group. (b) Normalized differential transmission of the signal beam, $\Delta T/T$, is shown *versus* time for CuO particles. The inset shows the focusing property of microspheres. Reproduced with permission from ref. 262. Copyright 2016, American Chemical Society. (c) Schematic of a mid-wave infrared detector, the simulated field distribution for a PNJ-assisted photodetector, and photocurrent enhancement factors. Reproduced with permission from ref. 265. Copyright 2016, American Institute of Physics. (d) Representative bird's eye corneal crater images and histology images for one-, three-, and five-sphere probes at 0.1 mJ. Reproduced with permission from ref. 268. Copyright 2012, Society of Photographic Instrumentation Engineers. (e) Schematic of the coherent Raman endoscope and SEM images of microsphere lens inserted into the hollow fiber core. Reproduced with permission from ref. 269. Copyright 2018, Nature Publishing Group. (f) Schematic and spectral current curves of the WGMs-assisted solar cell system. Reproduced with permission from ref. 277. Copyright 2011, John Wiley & Sons, Inc. (g) Schematic of leaf-inspired graphene/Si solar cell with a bilayer configuration of silica/titania nanoparticles on graphene. Reproduced with permission from ref. 284. Copyright 2019, Elsevier.

different materials, having diverse radii, revealed switching energies as low as 300 fJ and switching times as short as 350 fs, respectively.[262] See one of the representative experimental results in Fig. 11(b). These works demonstrate the great potential of non-resonance energy concentration induced by dielectric microspheres in all-optical manipulation. As for the goal of an integrable component, we believe the non-spherical PNJ generators designed from either simple geometries or inverse optimization, can achieve similar performance as that of microspheres in optical switching.

Enhanced photodetector. Typical photodiodes make a trade-off between high speed and high responsivity by varying the photodiode area. To achieve both high speed and high responsivity, it becomes necessary to concentrate the incident light into a subwavelength active volume region.[263] A dielectric microsphere, for instance, can be placed in front of a photodiode to concentrate the light energy down to the size of 0.0045 μm^3. This scheme is similar to the Shack–Hartmann wavefront sensor,[264] in which a microlens array is utilized to focus the incoming light to the photodetector with calibrated quadrants, but a significant difference is that the PNJ generated by microspheres can be operated in the nearfield domain. Allen *et al.* validated the feasibility of PNJ-enhanced photodetector mechanism by observing up to 100 times enhancement of sensitivity in the 2–5 μm range using PNJs produced by microspheres with different materials and with diverse diameters.[265] A typical mid-wave infrared detector grown on a GaSb substrate with an InAs/InAsSb type-II strained-layer superlattice (SLS) as the active materials is illustrated in Fig. 11(c). No concentrating elements are mounted on top of the detector, and thus the photocurrent is purely determined by the effective size of the active area of the detector. By mounting a dielectric microsphere with proper size and index on top of the active area, more energy can be concentrated to the active area [see the numerical simulation in the middle of Fig. 11(c)]. Thus, a significant enhancement of the photocurrent was achieved; see the current enhancement curves in Fig. 11(c). Because of the increased contact area for light, an angle-of-view up to 20° is achievable through this mechanism. As has been emphasized above, microspheres are not compatible with traditional semiconductor manufacturing processes; thus, PNJ generators designed with standard materials and non-spherical geometries are preferred. These can be either chosen from the standard photonics library or designed by inverse optimization approaches, as mentioned in Sec. 2.

Optical surgery. The laser has a long history of usage in ophthalmic surgery, *i.e.*, to reshape the surface of the eye. This is done to correct myopia (short-sightedness), hypermetropia (long sightedness) and astigmatism (uneven curvature of the eye's surface). The effectiveness and precision of the surgery are dominated by several factors including the penetration depth of laser, the spot diameter, and the laser power. Compared to conventional methods, a microsphere or a microsphere chain can provide more precise tissue removal by combining a small spot diameter with a short optical penetration depth.[266,267] It has been shown that one-, three-, and five-microsphere chain structures can result in different FWHM diameters in air, and that single Er:YAG pulses of 0.1 mJ and 75 μs duration can produce ablation craters with average diameters of 44, 30, and 17 μm and depths of 26, 10, and 8 μm, for one-, three-, and five-sphere structures, respectively.[268] The spatial filtering capability of dielectric microspheres is the key to providing spot diameters not otherwise available with conventional fiber systems. From the bird's eye corneal crater images and histology images for one-, three-, and five-sphere probes at 0.1 mJ as shown in the right sub-figures of Fig. 11(d), one can clearly find the difference in ablation caused by the different lengths of microsphere chains. The benefit from the superlensing effect of microspheres, nonlinear optics effect can be enhanced in biomaterials. This facilitates the development of novel *in vivo* diagnosis instruments such as the coherent Raman endoscope.[269] See the schematic of the endoscope along with the SEM images of the fiber core decorated with a microsphere lens in Fig. 11(e). Up to now, PNJ-based laser surgery has mostly been applied to *in vivo* treatment with the dominant figures of merit being PNJ strength and FWHM, while many other useful PNJ properties such as phase lag and scattering cross-section have rarely been investigated. Moreover, it has been demonstrated that some human tissues and diseases (such as breast ductal carcinoma tissues,[270] cancer,[271] and anisotropy of protein[272]) are ultrasensitive to the polarization states of light.[273] This feature potentially paves the way for future research into PNJ-based polarimetry for the diagnosis and treatment of these and many other human diseases.

Enhanced transmission and absorption. Transmission and absorption enhancement are vital to many research and commercial areas in terms of efficiency improvement. For thin-film solar cells, light absorption is usually proportional to the film thickness. However, if freely propagating sunlight can be transformed into a guided mode,[274,275] the optical path length significantly increases and this results in enhanced light absorption within the cell.[276] It was shown that WGMs in dielectric spheres can be coupled into particular modes of a-Si thin-film solar cells and thereby significantly enhance the efficiency of the cells. See the schematic and the spectral current density shown in the top row of Fig. 11(f). The spectral position of the absorption enhancement can be easily tuned by varying the sphere diameter and lattice constant. Also, the number of resonances can potentially be increased to make the response more broadband by assembling arrays of spheres with different diameters.[277] In fact, one can consider mixing spheres with various indices to change the spectral features. Similar work was also conducted by Jin *et al.*, but a significant difference is that the non-resonance feature of the microspheres was utilized. Specifically, they mounted a silica microsphere on top of a solid-state film system. The generated PNJ enhanced the peak transmittance of the graphene oxide film by 38%. The tunable nonlinearity was investigated by varying the concentration of silica microspheres.[278] So far, both the non-resonance PNJs and WGMs generated by dielectric microspheres have enhanced the absorption of light in solar cell systems, but we should mention that they can be combined with resonance features of metallic materials,[279] to further enhance the transmittance and absorption for bulk and 2D materials in both linear and nonlinear regimes.[280,281] An interesting work

conducted by Patel *et al.* further demonstrated the feasibility of PNJ-assisted transmittance enhancement. They attached a dielectric microsphere to the tip of a cantilever-based hollow probe used in a near-field scanning optical microscope and observed an order of magnitude enhancement in the measured images.[282] We should mention that the application of microscale or nanoscale structures to enhance transmission and absorption is not exclusively engineered; Mother Nature has provided several examples. For example, leaves have adapted themselves to meet the essential prerequisite of funneling light energy efficiently and channeling it to the reaction centers to promote photosynthesis through hierarchical morphologies with optimized structures of various shapes and sizes. More examples can be found in the compound eyes of Robber flies and the generation of $CaCO_3$ polycrystal nanoparticles on the margins of leaves to enable Kerker effects.[283] These discoveries pave the way for a bioinspired strategy of efficient light collection such as single-layer nanoparticles or bilayer nanoparticles for designing a high-efficiency photovoltaic device; see the schematic of the new type of solar cells in Fig. 11(g).[284–286]

Nanoscale sensing. Sensing nanoscale objects such as particles, viruses, and molecules, is not exclusive to LSPR-based metallic structures, but dielectric structures also present great potential,[287] especially those that can be excited in resonance modes such as ring and sphere resonators.[288] For non-resonance dielectric microspheres, the backscattering intensity of nanoparticles can be enhanced up to eight orders of magnitude when the particles are located within the PNJ.[289] Moreover, the PNJ-enhanced backscattering is extremely sensitive to the size of the nanoparticle.[290] This enhancement exists because the backscattering intensity of a well-positioned nanoparticle is proportional to the third power of its size parameter,[291] whereas the Rayleigh scattering of the same nanoparticle is proportional to the sixth power of its size parameter. Such a preliminary work opens the door to using a PNJ as a probe to sense nanoscale features without suffering the drawbacks of LSPR-based methods. Heifetz *et al.*, Zhao *et al.*, Kong *et al.*, and Yang *et al.* experimentally validated the enhanced backscattering at microwave and visible light frequencies.[292–295] It was found that increased backscattering is strongly dependent upon the illumination wavelength and the numerical aperture of the imaging system. The back-scattering-based sensing of nanoparticles can be controlled *via* the method of optical bonding, for instance, the microsphere being bonded to the tip of a microfiber can be positioned and controlled precisely to sense both nanoparticles and biomolecules.[296] See the optical images showing the sensed nanoparticles and plasmid DNA molecules as well as the measured reflection signals showing the dynamics of sensing in Fig. 12(a). To enable simultaneous sensing of multiple objects, one can create a PNJ array and measure (or image) the scattering information in either reflection or transmission mode. Ghenuche *et al.* utilized a microsphere array to sense fluorescence molecules at the picomolar concentration.[297] Using optical microscopy, Yang *et al.* dynamically detected Au and fluorescent nanoparticles in liquid medium using a microsphere array that was patterned in a microwell array template.[298] Au nanoparticles

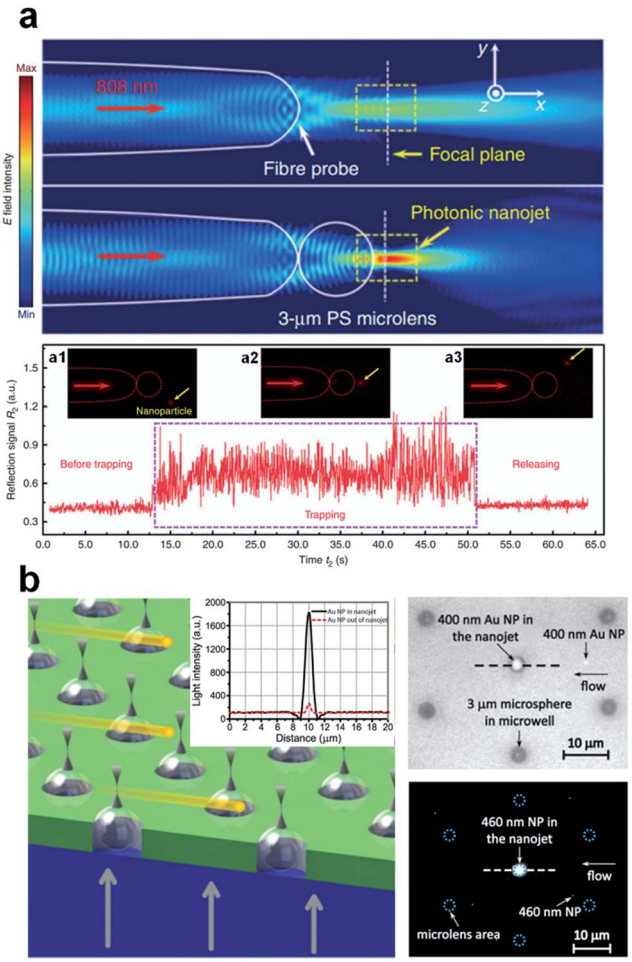

Fig. 12 (a) The real-time trace of the reflected 808 nm signal in the trapping process of an 85 nm fluorescent nanoparticle, and optical images showing the dynamic trapping of nanoparticles and plasmid DNA molecules. The insets in the bottom sub-figure of (a) show the fluorescent images (a1) before trapping, (a2) during trapping, and (a3) in the release. Reproduced with permission from ref. 296. Copyright 2016, Nature Publishing Group. (b) Schematic illustration of the optical detection of nanoparticles, and optical images showing the detected nanoparticles by the PNJ array. Reproduced with permission from ref. 298. Copyright 2015, American Chemical Society.

down to 50 nm in size, as well as fluorescent nanoparticles down to 20 nm in size, were observed using an optical microscope in bright-field or fluorescence mode, respectively. See the schematic of the sensing system as well as the detected nanoparticles in Fig. 12(b). To date, most PNJ-based sensors are made by microspheres or their derivatives. However, we believe, microscale or nanoscale structures with optimized non-spherical shapes using the techniques in Sec. 2 can also behave as non-resonance-based nanoscale sensors.

3.3 Gradient field in PNJs

What accompanies a narrow PNJ is a fast divergence of angular components, leading to an intense gradient field. Thus, a strong trapping potential can form around the hot spot, making the manipulation of nanoscale and microscale objects feasible in

a sub-wavelength volume. Different from conventional optical tweezers that are diffraction-limited, the ultra-narrow PNJs and resonance feature of microspheres may lead to unique trapping stiffnesses and efficiencies. Stable self-bonding and self-ordering is thus feasible even for biomaterials such as cells and viruses. The tunable parameters of PNJs (*e.g.*, FWHM, length, and working distance) even make *in vivo* manipulation of objects possible. For all these reasons, a comprehensive review on PNJ-based optical manipulation is vital.

Optical manipulation. Since the invention by Ashkin and co-workers from the 1970s onwards, optical tweezers have been extensively used in various research fields including biology,[299,300] materials engineering,[301,302] and atomic physics.[303] The trapping force arises from the strong focus-induced intensity gradient. This makes macroscale high-NA lenses popular tools for optical trapping. PNJs also have remarkable intensity gradients around their foci. This facilitates the manipulation of individual objects with nanoscale positioning accuracy.[304] Moreover, the nearfield and sub-diffraction-limit features of PNJs enables the manipulation of objects smaller than 100 nm. Li *et al.* used PNJs to perform the manipulation and detection of single objects including a single 85 nm fluorescent polystyrene nanoparticle and a plasmid DNA molecule.[296] They detected the backscattering and fluorescent signals and found that the enhancement factors are up to $\sim 10^3$ and ~ 30, respectively. The schematic and optical image shown in Fig. 13(a) illustrate the manipulation and detection of a single nanoparticle by a microsphere adhered to the tip of a fiber *via* optical bonding. They used the same concept to fabricate a trapping array rather than an individual microsphere on the tip of a thick fiber, to trap and manipulate diverse objects including *E. coli* cells, nanoparticles, and red blood cells.[305] See the optical images of trapping dynamics shown in Fig. 13(b). These cases demonstrate that PNJs are indeed a powerful tool for nanoparticle assembly, biosensing, single-cell analysis, and optical sorting. Relying on the concept of fiber-based optical tweezers, Li *et al.* fabricated a microfiber with a graphene-coated tip.[306] They demonstrated that thermal-gradient-induced natural convection flow and thermophoresis can trap the erythrocytes under low incident power, and the optical scattering force can arrange them precisely under higher incident power. Fig. 13(c) presents the sequences of optical microscope images recorded for erythrocyte arrangement based on the PNJ's pushing ability. Essentially speaking, the self-bonding among the trapped spherical particles arises from the generated PNJs and the propagating feature of beam in a sphere chain. The concept of fiber-based optical manipulation can be extended to a case with two fiber excitation, by which a single or multiple cells in solutions can be trapped and rotated bidirectionally under the action of optical forces.[307] A very recent study using a similar principle shows that a single cell can be bonded to the tip of a fiber *via* optical trapping for subdiffraction-limit imaging and manipulation of nano-objects. Shakhov *et al.* reported the effect of laser cavitation in water initiated by femtosecond pulses confined into the subwavelength PNJs of spherical microparticles. They combined this technique with optical trapping for cyclic particle movements and estimated a peak velocity and an acceleration acquired by microspheres propelled by PNJ cavitation. This provides a strategy for nondestructive optical micromanipulation, cavitation-assisted drug delivery, and laser energy transduction in microdevices.[308] In addition to the experimental validation, diverse theoretical and numerical investigations have been conducted on the PNJ-assisted optical manipulation, which may help to catalyze new directions for optical manipulation.[308–312] Although currently there are quite a lot of techniques to position microspheres for nanoscale fabrication, spherical shapes are difficult to achieve and/or to integrate together when using conventional top-down fabrication techniques, making the microsphere-based nanopatterning inconvenient. For those reasons, one can consider using the advanced inverse design tools mentioned in Sec. 2.5 to design microscale or nanoscale structures (as alternatives to microspheres) that are compatible with standard fabrication techniques like e-beam lithography. The properties (*e.g.*, focal length, strength, and working distance) of PNJs generated by those structures can be predesigned by tuning the controlling

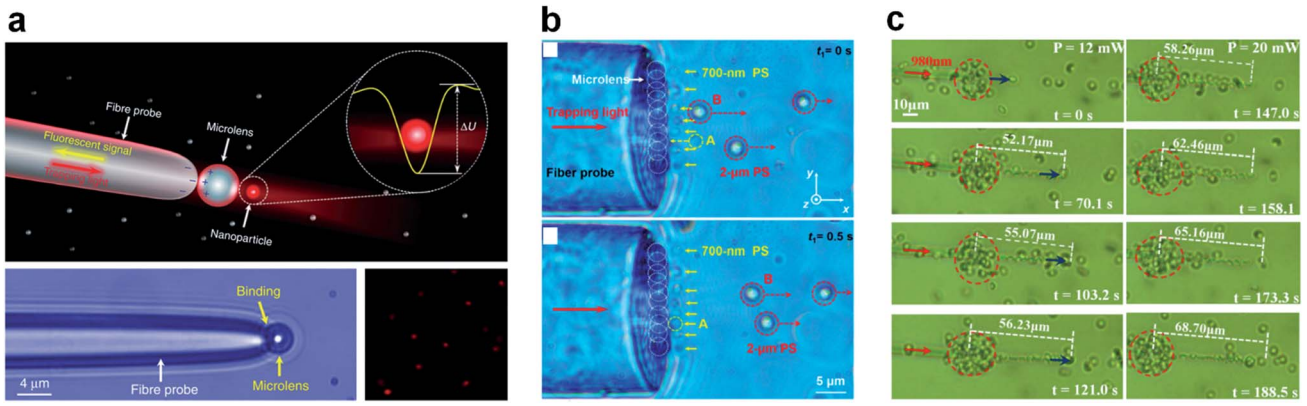

Fig. 13 (a) Schematic and experimental optical images of the microlens-based optical manipulation system. Reproduced with permission from ref. 296. Copyright 2016, Nature Publishing Group. (b) Selective trapping of polystyrene (PS) nanoparticles from a mixture of 700 nm and 2 μm PS particles. Reproduced with permission from ref. 305. Copyright 2016, American Chemical Society. (c) Erythrocyte trapping and arrangement processes at different instances of time as the incident power increases to 12 mW and 20 mW, respectively. Reproduced with permission from ref. 306. Copyright 2018, Optical Society of America.

parameters in the inverse design tools, making it possible to pattern both 2D and 3D devices inside the volume.

3.4 Microlensing, resonance, and self-bonding effects

A dielectric microsphere can be regarded as a microlens under the excitation of a plane wave. A cascade of microspheres with tailored indices, dimensions, and positions can behave as an optical imaging system consisting of multiple 4F components. Electromagnetic energy thus propagates through such a cascaded system in a periodically "convergence–divergence" manner. The resonance feature of microspheres can also enable low-loss waveguiding effects and even sharp bending for a cascade of contacted microspheres. Self-bonding that originates from trapping potential of PNJs enables the automatic formation of waveguides in liquid environments. We now review emerging applications of PNJ-based waveguides.

Waveguides. In ring resonators with multiple loops, we know that optical energy can propagate from one loop to another *via* nearfield coupling. Similar phenomenon can also happen in microspheres and microcylinders because of the well-known WGM coupling.[313] This enables microsphere or microcylinder chains to potentially serve as low loss waveguides. Deng *et al.* demonstrated light propagation by WGMs through a chain of coupled cylinder resonators, and observed a strong dependence of the speed of such propagation on the inter-resonator gap size and the overlap of the evanescent WGMs of two neighboring resonators.[314] Similar investigations have also been implemented by a rigorous integral equation method.[315] In fact, the resonance feature of microspheres or microcylinder indicates that the high-efficiency coupling and propagation of optical energy in a chain can be achieved at specific resonance wavelengths.[316] For this reason, coherent photon coupling, order and disorder effects in chains of coupled resonators were studied both theoretically and experimentally.[317,318] Specifically, a 2D analysis of finite-sized straight and curved coupled resonator optical waveguide (CROW) sections based on a rigorous Muller boundary integral equation method was implemented and showed that an ultra-low loss waveguide bend is achievable by selecting specific bend

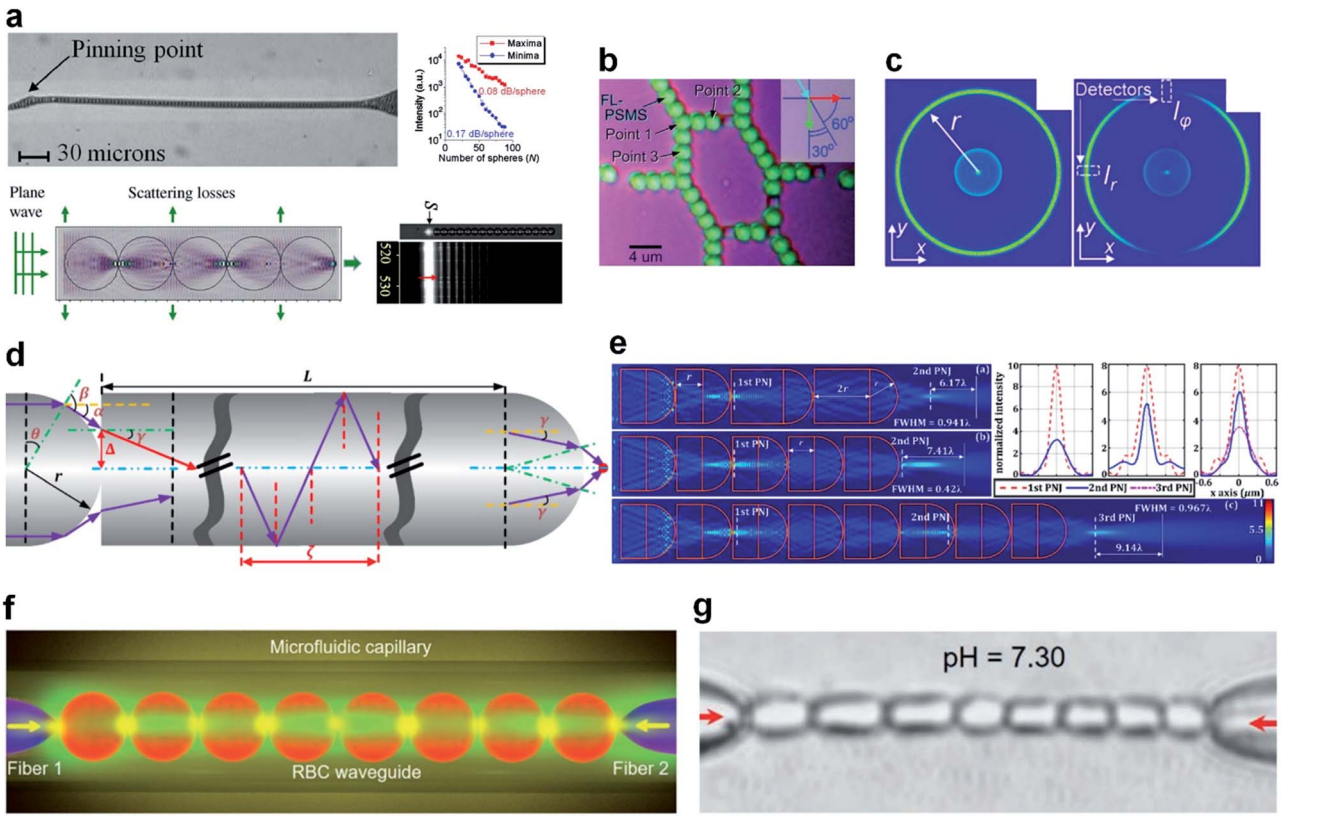

Fig. 14 (a) Optical image of a chain consisting of 5.0 μm microspheres, and representative numerical and experimental figures for a waveguide chain. Reproduced with permission from ref. 319. Copyright 2008, American Institute of Physics. (b) Optical microscope image of microsphere coupled-resonator optical waveguides with branched structures. Reproduced with permission from ref. 322. Copyright 2010, John Wiley & Sons, Inc. (c) Cross-section intensity distribution obtained at the end of a chain of 20 spheres with $n = 1.71$ as a result of illumination with collimated rays, and cross-section intensity distribution with the polarizer installed also showing positions of two detectors (dashed rectangles) used for degree-of-freedom calculations. Reproduced with permission from ref. 324. Copyright 2013, Optical Society of America. (d) Illustrated diagram showing the effect of the length L and hemispherical radius r on the focus property and (e) spatial intensity distribution maps showing the effect of length L and number of cascaded elements on the optical transport, and comparisons of the PNJ hot-spot cross-sectional profiles corresponding to the right-hand side sub-figures. Reproduced with permission from ref. 92. Copyright 2016, Optical Society of America. (f and g) Schematic and real optical images of the cell waveguide generated by two fiber probes in a microfluidic capillary. Reproduced with permission from ref. 326. Copyright 2019, John Wiley & Sons, Inc.

angles depending on the azimuthal order of the WGM and tuning the radius of the microdisk positioned at the CROW bends.[313] Although light propagation may not be as efficient when off resonance as when on resonance, low-loss waveguide propagation in the chain is still achievable for specific dimensions or structures in the form of PNJs. Yang *et al.* demonstrated that the periodical focusing of light in straight chains of touching 5 μm polystyrene microspheres can result in Fabry–Pérot fringes in the transmission spectrum with propagation losses of only 0.08 dB per sphere.[319] See Fig. 14(a). This indicates that PNJ-induced modes can also result in low-loss waveguide propagation,[320] provided that the dimension of microspheres is properly chosen.[321] The spectrum features capturing for a micro-demultiplexer of a CROW composed of polystyrene microspheres was also investigated.[322] The results show that microspheres can be assembled in a complex manner that contains multiple branches without suffering high loss. See the assembled microspheres with complex bending and joints in Fig. 14(b). Such a feature of small bending loss has also been investigated for microsphere chains with rounded small-angle bend.[323] An interesting work by Darafsheh *et al.* shows that chains of dielectric spheres and cylinders, rather than behaving as waveguide, can also act as polarizers [see Fig. 14(c)].[324] It is not surprising that the properties of microsphere chains can also be found in microcylinder chains *via* analogy, but the 2D feature of microcylinder chains has been demonstrated to have unusual features characterized in terms of supermodes.[325] Although structures with spherical shapes are more common for optical chain waveguides, investigations have also demonstrated that low-loss propagation with narrow beam waist is still possible using chains consisting of non-spherical elements.[92] See the schematic of beam propagation in a cascaded structure with bullet-shaped elements in Fig. 14(d), which is characterized by geometrical optics. Numerical investigations for chains with different numbers of bullets are shown in Fig. 14(e), in which low-loss and stable beam propagation is clearly visible. This preliminary investigation makes us believe that chain waveguides with even lower propagation loss and fabrication-compatible features can be designed by the aforementioned inverse design algorithms and be a promising future research direction. In contrast to the conventional waveguides consisting of inorganic materials, living biomaterials such as red blood cells, viruses, and yeast cells can be natural building blocks for biowaveguides through optical tweezing and self-bonding effects; see a representative biowaveguides consisting of ellipsoidal red blood cells in Fig. 14(f) and (g).[326] Biowaveguides that suffer from high propagation loss due to the irregular shapes and unknown material constituents of building blocks are to be expected. However, the self-assembly nature in various liquid environments make biowaveguides attractive in diverse fields such as *in vivo* sensing and turbid photonics.

Conclusions and outlook

This article reviewed many recent developments in the design of PNJ generators as well as the diverse applications based on PNJs. The conventional approaches to engineer the properties of PNJs, including the index- and geometry-based ones, have been thoroughly discussed and the dynamically controllable PNJ generation mechanisms, although rarely investigated, have been highlighted to remind readers of their importance. Natural materials that behave as PNJ generators have been discussed to enlighten future exploration in bio-inspired nanotechnology. Novel principles and frameworks, including the focusing for Bloch surface waves and plasmonic resonances as well as the pixel-based and density-based general inverse design mechanisms, have expanded the territory of PNJs tremendously. For a dielectric material with an arbitrary refractive index, researchers can now easily design ultra-narrow, elongated, highly concentrated, multiple, or any other types of PNJs. Therefore, we personally forecast two potentially important topics relating to the design of PNJs. The first is the dynamic tuning of PNJs for diverse applications *via* mechanisms like controllable liquid crystal molecules. The dynamic range of index or geometry control determines the tuning range of the generated PNJs. Thus, we believe this dynamic range should be treated as a significant benchmark when exploring new physical mechanisms for generating PNJs. The second is the generalized frameworks for inverse PNJ design. The vast degrees of freedom in these design frameworks together with 3D fabrication techniques such as grayscale lithography facilitate the generation of diverse PNJs beyond the conventional limitations such as $n < 2$ and beyond the standard geometries such as spheres and cuboids.

The scientific and engineering applications of PNJs are even more exciting. We have witnessed a bloom arising from the use of PNJs across diverse disciplines. The highly concentrated energy in PNJs may catalyze the re-examination of light–matter interactions, but the unique resonant and mode features in standard geometries like spheres and cylinders, are also responsible for the prosperity. Optical nanoscopy, nanoscale fabrication, optical data storage, enhanced Raman scattering, waveguide chains, and enhanced sensing, are conventionally understandable areas where PNJs contribute significantly, but recent works by multiple research groups and the introduction of non-spherical schemes have pushed those areas to an even higher level. The imaging limit of microsphere-assisted nanoscopy is still being pushed forward; the nanopatterning has been expanded from 2D to 3D; up to 0.08 dB loss per sphere has been experimentally demonstrated in a microsphere chain; and several orders of magnitude enhancement in Raman scattering and sensing have been observed in both resonance and non-resonance modes. The extension to other areas like laser surgery and optical manipulation, offers the possibility of combing PNJs with conventional instruments like Mueller matrix polarimeters and optical tweezers, to enable the enhanced performance as well as the new working modalities. The combination of multiple features of PNJs enables multifunctional devices such as the one combining gradient field and enhanced backscattering for achieving self-bonding of cells and dynamic sensing of nanoparticles in the same microchamber. We have noticed an important trend that PNJs are becoming critical in several areas that are dominated by nonlinear optics, such as all-optical switching and laser machining. We believe the applications of PNJs in nonlinear optics will keep growing as

it has in linear optics. At the end, we should emphasize that the generalized inverse PNJ design mechanisms as well as bio-inspired PNJs will undoubtedly contribute to the diverse applications of PNJs in terms of manufacturability, compatibility, and generalizability, which are critical to many fields such as semiconductors, photonics, and biomedicine.

Conflicts of interest

There are no conflicts to declare.

Acknowledgements

This work was funded by Cisco Systems Inc. (gift awards CG 1141107 and CG 1377144), University of Illinois at Urbana-Champaign College of Engineering Strategic Research Initiative, and Zhejiang University – University of Illinois at Urbana-Champaign (ZJUI) Institute Research Program. We acknowledge Cisco System Inc. for access to its Arcetri cluster. L. L. G. acknowledges the Center for Advanced Study at the University of Illinois for teaching release time.

Notes and references

1 D. K. Gramotnev and S. I. Bozhevolnyi, *Nat. Photonics*, 2010, **4**, 83–91.
2 J. B. Khurgin, *Nat. Nanotechnol.*, 2015, **10**, 2–6.
3 D. R. Smith, J. B. Pendry, M. C. K. Wiltshire and X. Zhang, *Science*, 2004, **305**, 788–792.
4 J. N. Anker, W. P. Hall, O. Lyandres, N. C. Shah, J. Zhao and R. P. Van Duyne, *Nat. Mater.*, 2008, **7**, 442–453.
5 A. G. Brolo, *Nat. Photonics*, 2012, **6**, 709–713.
6 T. Harter, S. Muehlbrandt, S. Ummethala, A. Schmid, S. Nellen, L. Hahn, W. Freude and C. Koos, *Nat. Photonics*, 2018, **12**, 625–633.
7 M. Schnell, P. Alonso-González, L. Arzubiaga, F. Casanova, L. E. Hueso, A. Chuvilin and R. Hillenbrand, *Nat. Photonics*, 2011, **5**, 283–287.
8 H. Choo, M. K. Kim, M. Staffaroni, T. J. Seok, J. Bokor, S. Cabrini, P. J. Schuck, M. C. Wu and E. Yablonovitch, *Nat. Photonics*, 2012, **6**, 838–844.
9 H. Im, H. Shao, Y. Il Park, V. M. Peterson, C. M. Castro, R. Weissleder and H. Lee, *Nat. Biotechnol.*, 2014, **32**, 490–495.
10 Z. Liu, S. Durant, H. Lee, Y. Pikus, N. Fang, Y. Xiong, C. Sun and X. Zhang, *Nano Lett.*, 2007, **7**, 403–408.
11 S. Law, L. Yu, A. Rosenberg and D. Wasserman, *Nano Lett.*, 2013, **13**, 4569–4574.
12 F. Yesilkoy, E. R. Arvelo, Y. Jahani, M. Liu, A. Tittl, V. Cevher, Y. Kivshar and H. Altug, *Nat. Photonics*, 2019, **13**, 390–396.
13 Y. T. Kim, H. Min, J. Lee, H. Park and C. Y. Lee, *Nanoscale*, 2018, **10**, 1030–1037.
14 P. Albella, M. A. Poyli, M. K. Schmidt, S. A. Maier, F. Moreno, J. J. Sáenz and J. Aizpurua, *J. Phys. Chem. C*, 2013, **117**, 13573–13584.
15 M. R. Shcherbakov, P. P. Vabishchevich, A. S. Shorokhov, K. E. Chong, D.-Y. Choi, I. Staude, A. E. Miroshnichenko, D. N. Neshev, A. A. Fedyanin and Y. S. Kivshar, *Nano Lett.*, 2015, **15**, 6985–6990.
16 R. Regmi, J. Berthelot, P. M. Winkler, M. Mivelle, J. Proust, F. Bedu, I. Ozerov, T. Begou, J. Lumeau, H. Rigneault, M. F. García-Parajó, S. Bidault, J. Wenger and N. Bonod, *Nano Lett.*, 2016, **16**, 5143–5151.
17 N. I. Zheludev, *Nat. Mater.*, 2008, **7**, 420–422.
18 G. Chen, Y. Li, X. Wang, Z. Wen, F. Lin, L. Dai, L. Chen, Y. He and S. Liu, *IEEE Photonics Technol. Lett.*, 2016, **28**, 335–338.
19 A. M. H. Wong and G. V. Eleftheriades, *Sci. Rep.*, 2015, **5**, 1–6.
20 V. R. Almeida, Q. Xu, C. A. Barrios and M. Lipson, *Opt. Lett.*, 2004, **29**, 1209.
21 Q. Xu, V. R. Almeida, R. R. Panepucci and M. Lipson, *Opt. Lett.*, 2004, **29**, 1626.
22 B. S. Luk'yanchuk, R. Paniagua-Domínguez, I. Minin, O. Minin and Z. Wang, *Opt. Mater. Express*, 2017, **7**, 1820.
23 A. V. Itagi and W. A. Challener, *J. Opt. Soc. Am. A*, 2005, **22**, 2847.
24 A. Heifetz, S.-C. Kong, A. V. Sahakian, A. Taflove and V. Backman, *J. Comput. Theor. Nanosci.*, 2009, **6**, 1979–1992.
25 Q. Li, M. Davanço and K. Srinivasan, *Nat. Photonics*, 2016, **10**, 406–414.
26 Z. Wang, W. Guo, L. Li, B. Luk'Yanchuk, A. Khan, Z. Liu, Z. Chen and M. Hong, *Nat. Commun.*, 2011, **2**, 216–218.
27 Y. Ben-Aryeh, *Appl. Phys. B: Lasers Opt.*, 2012, **109**, 165–170.
28 Y. Ben-Aryeh, *J. Opt. Soc. Am. A*, 2016, **33**, 2284.
29 Y. Ben-Aryeh, *Appl. Phys. B: Lasers Opt.*, 2006, **84**, 121–124.
30 Y. Ben-Aryeh, *Appl. Phys. B: Lasers Opt.*, 2008, **91**, 157–165.
31 H. Yang, R. Trouillon, G. Huszka and M. A. M. Gijs, *Nano Lett.*, 2016, **16**, 4862–4870.
32 H. H. Nguyen Pham, S. Hisatake, I. V. Minin, O. V. Minin and T. Nagatsuma, *Appl. Phys. Lett.*, 2016, **108**, 191102.
33 I. V. Minin, O. V. Minin, D. S. Ponomarev and I. A. Glinskiy, *Ann. Phys.*, 2018, **530**, 1800359.
34 Y. E. Geints, O. V. Minin and I. V. Minin, *Ann. Phys.*, 2019, 1900033.
35 L. Yue, B. Yan and Z. Wang, *Opt. Lett.*, 2016, **41**, 1336.
36 A. Rueda, F. Sedlmeir, M. Kumari, G. Leuchs and H. G. L. Schwefel, *Nature*, 2019, **568**, 378–381.
37 U. Keller, *Nature*, 2003, **424**, 831–838.
38 N. Savage, *Nat. Photonics*, 2009, **3**, 114–115.
39 G. Epple, K. S. Kleinbach, T. G. Euser, N. Y. Joly, T. Pfau, P. S. J. Russell and R. Löw, *Nat. Commun.*, 2014, **5**, 4132.
40 Z. Chen, A. Taflove and V. Backman, *Opt. Express*, 2004, **12**, 1214.
41 X. Li, Z. Chen, A. Taflove and V. Backman, *Opt. Express*, 2005, **13**, 526.
42 J. Zhu and L. L. Goddard, *IEEE Photonics Technol. Lett.*, 2018, **30**, 75–78.
43 A. D. Kiselev and D. O. Plutenko, *Phys. Rev. A*, 2014, **89**, 043803.

44 J. A. Gonzaga-Galeana and J. R. Zurita-Sánchez, *Journal of Electromagnetic Waves and Applications*, 2018, **32**, 1106–1125.
45 A. V. Itagi and W. A. Challener, *J. Opt. Soc. Am. A*, 2005, **22**, 2847.
46 S. Tadepalli, J. M. Slocik, M. K. Gupta, R. R. Naik and S. Singamaneni, *Chem. Rev.*, 2017, **117**, 12705–12763.
47 C. B. Lin, Z.-H. Huang and C.-Y. Liu, *Opt. Lett.*, 2019, **44**, 667.
48 J. N. Monks, B. Yan, N. Hawkins, F. Vollrath and Z. Wang, *Nano Lett.*, 2016, **16**, 5842–5845.
49 N. Schuergers, T. Lenn, R. Kampmann, M. V. Meissner, T. Esteves, M. Temerinac-Ott, J. G. Korvink, A. R. Lowe, C. W. Mullineaux and A. Wilde, *Elife*, 2015, **5**, e12620.
50 J. Zhu, Y. Liu, X. Yu, R. Zhou, J.-M. Jin and L. L. Goddard, *Nano Lett.*, 2019, **19**, 5347–5355.
51 J. Zhu, R. Zhou, L. Zhang, B. Ge, C. Luo and L. L. Goddard, *Opt. Express*, 2019, **27**, 6719.
52 Y. Li, X. Liu and B. Li, *Light: Sci. Appl.*, 2019, **8**, 61.
53 Y. Li, X. Liu, X. Yang, H. Lei, Y. Zhang and B. Li, *ACS Nano*, 2017, **11**, 10672–10680.
54 Y. Li, H. Xin, Y. Zhang, H. Lei, T. Zhang, H. Ye, J. J. Saenz, C.-W. Qiu and B. Li, *ACS Nano*, 2018, **12**, 10703–10711.
55 H. Xin, Y. Li, X. Liu and B. Li, *Nano Lett.*, 2013, **13**, 3408–3413.
56 X. Liu, Y. Li, X. Xu, Y. Zhang and B. Li, *ACS Appl. Bio Mater.*, 2019, **2**, 2889–2895.
57 L. Miccio, P. Memmolo, F. Merola, P. A. Netti and P. Ferraro, *Nat. Commun.*, 2015, **6**, 6502.
58 S. Wilhelm, *ACS Nano*, 2017, **11**, 10644–10653.
59 G. E. Arnaoutakis and B. S. Richards, *Opt. Mater.*, 2018, **83**, 47–54.
60 N. Yu, P. Genevet, M. A. Kats, F. Aieta, J. P. Tetienne, F. Capasso and Z. Gaburro, *Science*, 2011, **334**, 333–337.
61 S. Pérez-López, J. M. Fuster, I. V. Minin, O. V. Minin and P. Candelas, *Sci. Rep.*, 2019, **9**, 13363.
62 S.-C. Kong, A. Taflove and V. Backman, *Opt. Express*, 2009, **17**, 3722.
63 C. Yan, H. Ding and L. Dai, *Chin. Opt. Lett.*, 2010, **8**(7), 706–708.
64 Y. E. Geints, A. A. Zemlyanov and E. K. Panina, *J. Opt. Soc. Am. B*, 2011, **28**, 1825.
65 Y. Shen, L. V. Wang and J.-T. Shen, *Opt. Lett.*, 2014, **39**, 4120.
66 G. Gu, R. Zhou, Z. Chen, H. Xu, G. Cai, Z. Cai and M. Hong, *Opt. Lett.*, 2015, **40**, 625.
67 Z. Zhen, Y. Huang, Y. Feng, Y. Shen and Z. Li, *Opt. Express*, 2019, **27**, 9178.
68 X. Mao, Y. Yang, H. Dai, D. Luo, B. Yao and S. Yan, *Opt. Express*, 2015, **23**, 26426.
69 J. P. F. Lagerwall and G. Scalia, *Curr. Appl. Phys.*, 2012, **12**, 1387–1412.
70 G. H. Brown, *J. Electron. Mater.*, 1973, **2**, 403–430.
71 H. Kikuchi, M. Yokota, Y. Hisakado, H. Yang and T. Kajiyama, *Nat. Mater.*, 2002, **1**, 64–68.
72 R. Narayan, J. E. Kim, J. Y. Kim, K. E. Lee and S. O. Kim, *Adv. Mater.*, 2016, **28**, 3045–3068.
73 T. J. White and D. J. Broer, *Nat. Mater.*, 2015, **14**, 1087–1098.
74 C.-Y. Liu, *Phys. Lett. A*, 2014, **378**, 229–234.
75 T. Matsui and A. Okajima, *Jpn. J. Appl. Phys.*, 2014, **53**, 01AE04.
76 N. Eti, I. H. Giden, Z. Hayran, B. Rezaei and H. Kurt, *J. Mod. Opt.*, 2017, **64**, 1566–1577.
77 B. Du, J. Xia, J. Wu, J. Zhao, H. Zhang, B. Du, J. Xia, J. Wu, J. Zhao and H. Zhang, *Nanomaterials*, 2019, **9**, 72.
78 T. Matsui and K. Tsukuda, *Opt. Lett.*, 2017, **42**, 4663.
79 B. Gholipour, A. Karvounis, J. Yin, C. Soci, K. F. MacDonald and N. I. Zheludev, *NPG Asia Mater.*, 2018, **10**, 533–539.
80 C. Lan, H. Ma, M. Wang, Z. Gao, K. Liu, K. Bi, J. Zhou and X. Xin, *ACS Appl. Mater. Interfaces*, 2019, **11**, 14229–14238.
81 W. Aftab, X. Huang, W. Wu, Z. Liang, A. Mahmood and R. Zou, *Energy Environ. Sci.*, 2018, **11**, 1392–1424.
82 C. Chen, P. Jost, H. Volker, M. Kaminski, M. Wirtssohn, U. Engelmann, K. Krüger, F. Schlich, C. Schlockermann, R. P. S. M. Lobo and M. Wuttig, *Phys. Rev. B*, 2017, **95**, 094111.
83 Y. Yang, C.-T. Li, S. M. Sadeghipour, H. Dieker, M. Wuttig and M. Asheghi, *J. Appl. Phys.*, 2006, **100**, 024102.
84 J. H. Soh, M. Wu, G. Gu, L. Chen and M. Hong, *Appl. Opt.*, 2016, **55**, 3751.
85 V. Kumar, P. K. Goyal, S. Mahendia, R. Gupta, T. Sharma and S. Kumar, *Radiat. Eff. Defects Solids*, 2011, **166**, 109–113.
86 Y. Yu, Y. Yu, L. Huang, H. Peng, L. Xiong and L. Cao, *Nano Lett.*, 2017, **17**, 3613–3618.
87 D. S. Engstrom, B. Porter, M. Pacios and H. Bhaskaran, *J. Mater. Res.*, 2014, **29**, 1792–1816.
88 K. Du, I. Wathuthanthri, C.-H. Choi, K. Du, I. Wathuthanthri and C.-H. Choi, *Micromachines*, 2017, **8**, 275.
89 J. A. Liddle and G. M. Gallatin, *ACS Nano*, 2016, **10**, 2995–3014.
90 K. Kang, Y. Cho, K. Yu, K. Kang, Y. Cho and K. J. Yu, *Micromachines*, 2018, **9**, 263.
91 A. Polman and H. A. Atwater, *Nat. Mater.*, 2012, **11**, 174–177.
92 J. Zhu and L. L. Goddard, *Opt. Express*, 2016, **24**, 30444.
93 M.-S. Kim, T. Scharf, S. Mühlig, C. Rockstuhl and H. P. Herzig, *Opt. Express*, 2011, **19**, 10206.
94 Y. E. Geints, A. A. Zemlyanov and E. K. Panina, *Quantum Electron.*, 2011, **41**, 520–525.
95 D. Grojo, N. Sandeau, L. Boarino, C. Constantinescu, N. De Leo, M. Laus and K. Sparnacci, *Opt. Lett.*, 2014, **39**, 3989.
96 V. Pacheco-Peña and M. Beruete, *J. Appl. Phys.*, 2019, **125**, 084104.
97 Y. Huang, Z. Zhen, Y. Shen, C. Min and G. Veronis, *Opt. Express*, 2019, **27**, 1310.
98 S. Zhou, *Jpn. J. Appl. Phys.*, 2019, **58**, 050920.
99 Z. Hengyu, C. Zaichun, C. T. Chong and H. Minghui, *Opt. Express*, 2015, **23**, 6626.
100 D. McCloskey, J. J. Wang and J. F. Donegan, *Opt. Express*, 2011, **20**, 128.
101 M. X. Wu, B. J. Huang, R. Chen, Y. Yang, J. F. Wu, R. Ji, X. D. Chen and M. H. Hong, *Opt. Express*, 2015, **23**, 20096.
102 M. Wu, R. Chen, J. Soh, Y. Shen, L. Jiao, J. Wu, X. Chen, R. Ji and M. Hong, *Sci. Rep.*, 2016, **6**, 31637.

103 V. V. Kotlyar, S. S. Stafeev and A. Feldman, *Appl. Opt.*, 2014, **53**, 5322.
104 I. V. Minin, O. V. Minin, V. Pacheco-Peña and M. Beruete, *Opt. Lett.*, 2015, **40**, 2329.
105 D. McCloskey, K. E. Ballantine, P. R. Eastham and J. F. Donegan, *Opt. Express*, 2015, **23**, 26326.
106 L. Yue, B. Yan, J. N. Monks, Z. Wang, N. T. Tung, V. D. Lam, O. Minin and I. Minin, *J. Phys. D: Appl. Phys.*, 2017, **50**, 175102.
107 J. Yang, P. Twardowski, P. Gérard, Y. Duo, J. Fontaine and S. Lecler, *Opt. Express*, 2018, **26**, 3723.
108 Y. E. Geints, A. A. Zemlyanov, O. V. Minin and I. V. Minin, *J. Opt.*, 2018, **20**, 065606.
109 H. H. Nguyen Pham, S. Hisatake, O. V. Minin, T. Nagatsuma and I. V. Minin, *Appl. Phys. Lett.*, 2017, **110**, 201105.
110 B. Zhang, J. Hao, Z. Shen, H. Wu, K. Zhu, J. Xu and J. Ding, *Appl. Opt.*, 2018, **57**, 8331.
111 Y. E. Geints, A. A. Zemlyanov and E. K. Panina, *J. Opt. Soc. Am. B*, 2015, **32**, 1570.
112 Y. E. Geints and A. A. Zemlyanov, *J. Appl. Phys.*, 2016, **119**, 153101.
113 C.-Y. Liu, O. V. Minin and I. V. Minin, *Europhys. Lett.*, 2018, **123**, 54003.
114 S. A. Degtyarev, A. P. Porfirev and S. N. Khonina, *Appl. Opt.*, 2016, **55**, B44.
115 H. Zhang, H. Xia and Y. Zhao, *ACS Macro Lett.*, 2014, **3**, 940–943.
116 S. S. Walavalkar, A. P. Homyk, M. D. Henry and A. Scherer, *J. Appl. Phys.*, 2010, **107**, 124314.
117 C. Friese and H. Zappe, *J. Microelectromech. Syst.*, 2008, **17**, 11–19.
118 Q. Yan and Y. Zhao, *J. Am. Chem. Soc.*, 2013, **135**, 16300–16303.
119 S. Kee, N. Kim, B. Park, B. S. Kim, S. Hong, J.-H. Lee, S. Jeong, A. Kim, S.-Y. Jang and K. Lee, *Adv. Mater.*, 2018, **30**, 1703437.
120 D. Ju, H. Pei, Y. Jiang and X. Sun, *Appl. Phys. Lett.*, 2013, **102**, 171109.
121 V. Pacheco-Peña, I. V. Minin, O. V. Minin and M. Beruete, *Ann. Phys.*, 2016, **528**, 684–692.
122 I. V. Minin, O. V. Minin, D. S. Ponomarev and I. A. Glinskiy, *Ann. Phys.*, 2018, **530**, 1800359.
123 M. S. Kim, B. Vosoughi Lahijani, N. Descharmes, J. Straubel, F. Negredo, C. Rockstuhl, M. Häyrinen, M. Kuittinen, M. Roussey and H. P. Herzig, *ACS Photonics*, 2017, **4**, 1477–1483.
124 M.-S. Kim, A. Vetter, C. Rockstuhl, B. V. Lahijani, M. Häyrinen, M. Kuittinen, M. Roussey and H. P. Herzig, *Commun. Phys.*, 2018, **1**, 63.
125 Y. Augenstein, A. Vetter, B. V. Lahijani, H. P. Herzig, C. Rockstuhl and M.-S. Kim, *Light: Sci. Appl.*, 2018, **7**, 104.
126 A. Boriskin, V. Drazic, R. Keating, M. Damghanian, O. Shramkova and L. Blondé, *Opt. Lett.*, 2018, **43**, 4053.
127 M. P. Bendsøe and O. Sigmund, *Arch. Appl. Mech.*, 1999, **69**, 635–654.
128 O. Sigmund and J. Petersson, *Struct. Optim.*, 1998, **16**, 68–75.
129 O. Sigmund, *Struct. Multidiscip. Optim.*, 2001, **21**, 120–127.
130 O. Sigmund, *Mech. Struct. Mach.*, 1997, **25**, 493–524.
131 O. Sigmund, *Int. J. Solids Struct.*, 1994, **31**, 2313–2329.
132 C. B. W. Pedersen, T. Buhl and O. Sigmund, *Int. J. Numer. Methods Eng.*, 2001, **50**, 2683–2705.
133 M. Jansen, G. Lombaert, M. Diehl, B. S. Lazarov, O. Sigmund and M. Schevenels, *Struct. Multidiscip. Optim.*, 2013, **47**, 317–333.
134 P. I. Borel, A. Harpøth, L. H. Frandsen, M. Kristensen, P. Shi, J. S. Jensen and O. Sigmund, *Opt. Express*, 2004, **12**, 1996.
135 O. Sigmund and K. Hougaard, *Phys. Rev. Lett.*, 2008, **100**, 153904.
136 J. S. Jensen and O. Sigmund, *Appl. Phys. Lett.*, 2004, **84**, 2022–2024.
137 F. Wang, J. S. Jensen and O. Sigmund, *J. Opt. Soc. Am. B*, 2011, **28**, 387.
138 J. S. Jensen, O. Sigmund, L. H. Frandsen, P. I. Borel, A. Harpoth and M. Kristensen, *IEEE Photonics Technol. Lett.*, 2005, **17**, 1202–1204.
139 L. F. Frellsen, Y. Ding, O. Sigmund and L. H. Frandsen, *Opt. Express*, 2016, **24**, 16866.
140 R. Matzen, J. S. Jensen and O. Sigmund, *J. Opt. Soc. Am. B*, 2010, **27**, 2040.
141 M. B. Dühring, O. Sigmund and T. Feurer, *J. Opt. Soc. Am. B*, 2010, **27**, 51.
142 J. S. Jensen and O. Sigmund, *Laser Photonics Rev.*, 2011, **5**, 308–321.
143 L. H. Frandsen, A. Harpoth, P. I. Borel, M. Kristensen, J. S. Jensen and O. Sigmund, *Opt. Express*, 2004, **12**, 5916.
144 I. D. Mayergoyz, D. R. Fredkin and Z. Zhang, *Phys. Rev. B: Condens. Matter Mater. Phys.*, 2005, **72**, 155412.
145 A. E. Miroshnichenko, S. Flach and Y. S. Kivshar, *Rev. Mod. Phys.*, 2010, **82**, 2257–2298.
146 P. R. Wiecha, A. Cuche, A. Arbouet, C. Girard, G. Colas Des Francs, A. Lecestre, G. Larrieu, F. Fournel, V. Larrey, T. Baron and V. Paillard, *ACS Photonics*, 2017, **4**, 2036–2046.
147 K. C. Vernon, A. M. Funston, C. Novo, D. E. Gómez, P. Mulvaney and T. J. Davis, *Nano Lett.*, 2010, **10**, 2080–2086.
148 S. Wang and C. T. Chan, *Opt. Express*, 2016, **24**, 2235.
149 D. Vercruysse, Y. Sonnefraud, N. Verellen, F. B. Fuchs, G. Di Martino, L. Lagae, V. V. Moshchalkov, S. A. Maier and P. Van Dorpe, *Nano Lett.*, 2013, **13**, 3843–3849.
150 M. A. Yurkin and A. G. Hoekstra, *J. Quant. Spectrosc. Radiat. Transfer*, 2007, **106**, 558–589.
151 B. T. Draine and P. J. Flatau, *J. Opt. Soc. Am. A*, 1994, **11**, 1491.
152 B. T. Draine and P. J. Flatau, *J. Opt. Soc. Am. A*, 2008, **25**, 2693.
153 R. Schmehl, B. M. Nebeker and E. D. Hirleman, *J. Opt. Soc. Am. A*, 1997, **14**, 3026.
154 M. A. Yurkin, V. P. Maltsev and A. G. Hoekstra, *J. Opt. Soc. Am. A*, 2006, **23**, 2578.

155 M. A. Yurkin and M. Huntemann, *J. Phys. Chem. C*, 2015, **119**, 29088–29094.
156 A. Penttilä, E. Zubko, K. Lumme, K. Muinonen, M. A. Yurkin, B. Draine, J. Rahola, A. G. Hoekstra and Y. Shkuratov, *J. Quant. Spectrosc. Radiat. Transfer*, 2007, **106**, 417–436.
157 D. A. Smunev, P. C. Chaumet and M. A. Yurkin, *J. Quant. Spectrosc. Radiat. Transfer*, 2015, **156**, 67–79.
158 S. B. Singham and C. F. Bohren, *Opt. Lett.*, 1987, **12**, 10.
159 K. Svanberg, *Int. J. Numer. Methods Eng.*, 1987, **24**, 359–373.
160 L. Li and K. Khandelwal, *Eng. Struct.*, 2015, **85**, 144–161.
161 J. K. Guest, J. H. Prévost and T. Belytschko, *Int. J. Numer. Methods Eng.*, 2004, **61**, 238–254.
162 F. Wang, B. S. Lazarov and O. Sigmund, *Struct. Multidiscip. Optim.*, 2011, **43**, 767–784.
163 B. Shen, P. Wang, R. Polson and R. Menon, *Nat. Photonics*, 2015, **9**, 378–382.
164 A. Arbabi, Y. Horie, A. J. Ball, M. Bagheri and A. Faraon, *Nat. Commun.*, 2015, **6**, 7069.
165 Z. Zhen, Y. Huang, Y. Feng, Y. Shen and Z. Li, *Opt. Express*, 2019, **27**, 9178.
166 J. Zhu and L. L. Goddard, *Opt. Express*, 2016, **24**, 30444.
167 C. Balas, *Meas. Sci. Technol.*, 2009, **20**, 104020.
168 J. M. Schmitt, *IEEE J. Sel. Top. Quantum Electron.*, 1999, **5**, 1205–1215.
169 J. Y. Lee, B. H. Hong, W. Y. Kim, S. K. Min, Y. Kim, M. V. Jouravlev, R. Bose, K. S. Kim, I.-C. Hwang, L. J. Kaufman, C. W. Wong, P. Kim and K. S. Kim, *Nature*, 2009, **460**, 498–501.
170 L. Chen, Y. Zhou, Y. Li and M. Hong, *Appl. Phys. Rev.*, 2019, **6**, 021304.
171 L. Li, W. Guo, Y. Yan, S. Lee and T. Wang, *Light: Sci. Appl.*, 2013, **2**, e104.
172 L. A. Krivitsky, J. J. Wang, Z. Wang and B. Luk'yanchuk, *Sci. Rep.*, 2013, **3**, 3501.
173 A. Darafsheh, N. I. Limberopoulos, J. S. Derov, D. E. Walker and V. N. Astratov, *Appl. Phys. Lett.*, 2014, **104**, 061117.
174 A. Darafsheh, *Opt. Lett.*, 2017, **42**, 735.
175 H. Yang, N. Moullan, J. Auwerx and M. A. M. Gijs, *Small*, 2014, **10**, 1712–1718.
176 H. Zhu, W. Fan, S. Zhou, M. Chen and L. Wu, *ACS Nano*, 2016, **10**, 9755–9761.
177 X. Hao, C. Kuang, X. Liu, H. Zhang and Y. Li, *Appl. Phys. Lett.*, 2011, **99**, 203102.
178 X. Hao, X. Liu, C. Kuang, Y. Li, Y. Ku, H. Zhang, H. Li and L. Tong, *Appl. Phys. Lett.*, 2013, **102**, 013104.
179 B. Jia, F. Wang, H. Chan, G. Zhang and W. J. Li, *Microsyst. Nanoeng.*, 2019, **5**, 1.
180 J. Wenger, D. Gérard, H. Aouani and H. Rigneault, *Anal. Chem.*, 2008, **80**, 6800–6804.
181 M. Duocastella, F. Tantussi, A. Haddadpour, R. P. Zaccaria, A. Jacassi, G. Veronis, A. Diaspro and F. De Angelis, *Sci. Rep.*, 2017, **7**, 3474.
182 P. C. Montgomery, S. Lecler, A. Leong-Hoï and P. Pfeiffer, *J. Phys.: Conf. Ser.*, 2017, **794**, 012006.
183 Y. Zhou, Y. Tang, Q. Deng, L. Zhao and S. Hu, *Appl. Phys. Express*, 2017, **10**, 082501.
184 G. Huszka, H. Yang and M. A. M. Gijs, *Opt. Express*, 2017, **25**, 15079.
185 F. Wang, S. Yang, H. Ma, P. Shen, N. Wei, M. Wang, Y. Xia, Y. Deng and Y.-H. Ye, *Appl. Phys. Lett.*, 2018, **112**, 023101.
186 B. Hou and L. Zhang, *J. Opt.*, 2018, **20**, 055606.
187 S. Yang, X. Wang, J. Wang, Y. Cao, F. Wang, T. Chen and Y.-H. Ye, *Appl. Opt.*, 2018, **57**, 7818.
188 K. Meng, S. Gao, Z. Yang, H. Liu, T. Chen and L. Sun, *J. Phys.: Conf. Ser.*, 2018, **1074**, 012097.
189 Y. Xiong, Z. Liu, C. Sun and X. Zhang, *Nano Lett.*, 2007, **7**, 3360–3365.
190 X. Zhang and Z. Liu, *Nat. Mater.*, 2008, **7**, 435–441.
191 Z. Liu, S. Durant, H. Lee, Y. Pikus, N. Fang, Y. Xiong, C. Sun and X. Zhang, *Nano Lett.*, 2007, **7**, 403–408.
192 L. Li, F. Li and T. J. Cui, *Opt. Express*, 2014, **22**, 5431.
193 Z. Wen, Y. He, Y. Li, L. Chen and G. Chen, *Opt. Express*, 2014, **22**, 22163.
194 E. T. F. Rogers and N. I. Zheludev, *J. Opt.*, 2013, **15**, 094008.
195 A. N. Boettiger, B. Bintu, J. R. Moffitt, S. Wang, B. J. Beliveau, G. Fudenberg, M. Imakaev, L. A. Mirny, C. Wu and X. Zhuang, *Nature*, 2016, **529**, 418–422.
196 M. J. Rust, M. Bates and X. Zhuang, *Nat. Methods*, 2006, **3**, 793–796.
197 A. V. Maslov and V. N. Astratov, *Appl. Phys. Lett.*, 2017, **110**, 261107.
198 Y. Zhou, Y. Tang, Y. He, X. Liu and S. Hu, *Appl. Phys. Express*, 2018, **11**, 032501.
199 P.-Y. Li, Y. Tsao, Y.-J. Liu, Z.-X. Lou, W.-L. Lee, S.-W. Chu and C.-W. Chang, *Opt. Express*, 2016, **24**, 16479.
200 Y. Duan, G. Barbastathis and B. Zhang, *Opt. Lett.*, 2013, **38**, 2988.
201 R. C. Dunn, *Chem. Rev.*, 1999, **99**, 2891–2928.
202 M. Deubel, G. von Freymann, M. Wegener, S. Pereira, K. Busch and C. M. Soukoulis, *Nat. Mater.*, 2004, **3**, 444–447.
203 W. Gao, N. Singh, L. Song, Z. Liu, A. L. M. Reddy, L. Ci, R. Vajtai, Q. Zhang, B. Wei and P. M. Ajayan, *Nat. Nanotechnol.*, 2011, **6**, 496–500.
204 S. Wang and T. Ding, *Nanoscale*, 2019, **11**, 9593–9597.
205 Y. Wen, H. Yu, W. Zhao, F. Wang, X. Wang, L. Liu and W. J. Li, *IEEE Trans. Nanotechnol.*, 2019, **18**, 226–233.
206 K. Piglmayer, R. Denk and D. Bäuerle, *Appl. Phys. Lett.*, 2002, **80**, 4693–4695.
207 M. Mosbacher, H.-J. Münzer, J. Zimmermann, J. Solis, J. Boneberg and P. Leiderer, *Appl. Phys. A: Mater. Sci. Process.*, 2001, **72**, 41–44.
208 H.-J. Munzer, M. Mosbacher, M. Bertsch, J. Zimmermann, P. Leiderer and J. Boneberg, *J. Microsc.*, 2001, **202**, 129–135.
209 Y.-H. Chien, C.-H. Wang, C.-C. Liu, S.-H. Chang, K. V. Kong and Y.-C. Chang, *ACS Appl. Mater. Interfaces*, 2017, **9**, 24917–24925.
210 P. A. Bobbert and J. Vlieger, *Phys. A*, 1986, **137**, 209–242.
211 V. M. Sundaram and S.-B. Wen, *Appl. Phys. Lett.*, 2014, **105**, 204102.
212 P. Chýlek and J. Zhan, *Appl. Opt.*, 1990, **29**, 3984.

213 P. Ferrand, J. Wenger, A. Devilez, M. Pianta, B. Stout, N. Bonod, E. Popov and H. Rigneault, *Opt. Express*, 2008, **16**, 6930.
214 Y. Wen, H. Yu, W. Zhao, F. Wang, X. Wang, L. Liu and W. J. Li, *IEEE Trans. Nanotechnol.*, 2019, **18**, 226–233.
215 A. S. Dimitrov and K. Nagayama, *Langmuir*, 1996, **12**, 1303–1311.
216 J. Zhang, Y. Li, X. Zhang and B. Yang, *Adv. Mater.*, 2010, **22**, 4249–4269.
217 X. Chen, Z. Chen, N. Fu, G. Lu and B. Yang, *Adv. Mater.*, 2003, **15**, 1413–1417.
218 L. Li, W. Guo, Z. B. Wang, Z. Liu, D. Whitehead and B. Luk'yanchuk, *J. Micromech. Microeng.*, 2009, **19**, 054002.
219 D. G. Grier, *Nature*, 2003, **424**, 810–816.
220 S. Maruo, O. Nakamura and S. Kawata, *Opt. Lett.*, 1997, **22**, 132.
221 C.-H. Chang, L. Tian, W. R. Hesse, H. Gao, H. J. Choi, J.-G. Kim, M. Siddiqui and G. Barbastathis, *Nano Lett.*, 2011, **11**, 2533–2537.
222 R. Denk, K. Piglmayer and D. Bäuerle, *Appl. Phys. A: Mater. Sci. Process.*, 2003, **76**, 1–3.
223 B. P. Corgier and D. Bélanger, *Langmuir*, 2010, **26**, 5991–5997.
224 Y. Wu, L. Ji, Z. Lin, Q. Li and Y. Jiang, *Appl. Surf. Sci.*, 2015, **357**, 832–837.
225 W. N. Ng, C. H. Leung, P. T. Lai and H. W. Choi, *Nanotechnology*, 2008, **19**, 255302.
226 P. Gao, J. He, S. Zhou, X. Yang, S. Li, J. Sheng, D. Wang, T. Yu, J. Ye and Y. Cui, *Nano Lett.*, 2015, **15**, 4591–4598.
227 E. Mcleod and C. B. Arnold, *Nat. Nanotechnol.*, 2008, **3**, 413–417.
228 X. A. Zhang, I.-T. Chen and C.-H. Chang, *Nanotechnology*, 2019, **30**, 352002.
229 A. Jacassi, F. Tantussi, M. Dipalo, C. Biagini, N. Maccaferri, A. Bozzola and F. De Angelis, *ACS Appl. Mater. Interfaces*, 2017, **9**, 32386–32393.
230 J. Kato, N. Takeyasu, Y. Adachi, H.-B. Sun and S. Kawata, *Appl. Phys. Lett.*, 2005, **86**, 044102.
231 X. A. Zhang, J. Elek and C. H. Chang, *ACS Nano*, 2013, **7**, 6212–6218.
232 H. Nagai, A. Poteet, X. A. Zhang and C. H. Chang, *Nanotechnology*, 2017, **28**, 125302.
233 M. Wuttig, H. Bhaskaran and T. Taubner, *Nat. Photonics*, 2017, **11**, 465–476.
234 D. Xiang, T. Liu, J. Xu, J. Y. Tan, Z. Hu, B. Lei, Y. Zheng, J. Wu, A. H. C. Neto, L. Liu and W. Chen, *Nat. Commun.*, 2018, **9**, 2966.
235 Q. Zhang, Z. Xia, Y.-B. Cheng and M. Gu, *Nat. Commun.*, 2018, **9**, 1183.
236 S.-C. Kong, A. Sahakian, A. Taflove and V. Backman, *Opt. Express*, 2008, **16**, 13713.
237 F. M. Huang and N. I. Zheludev, *Nano Lett.*, 2009, **9**, 1249–1254.
238 H. J. Hyvärinen, S. Rehman, J. Tervo, J. Turunen and C. J. R. Sheppard, *Opt. Lett.*, 2012, **37**, 903.
239 M. V. Berry and M. R. Dennis, *J. Phys. A: Math. Theor.*, 2009, **42**, 22003.
240 S. Sun, L. Wu, P. Bai and C. E. Png, *Phys. Chem. Chem. Phys.*, 2016, **18**, 19324–19335.
241 Y. Zhang, Y. Yan, L. Yang, C. Xing, Y. Zeng, Y. Zhao and Y. Jiang, *Opt. Express*, 2019, **27**, 15399.
242 H.-J. Lin, K. de Oliveira Lima, P. Gredin, M. Mortier, L. Billot, Z. Chen and L. Aigouy, *Appl. Phys. Lett.*, 2017, **111**, 251109.
243 A. B. Vasista, S. Tiwari, D. K. Sharma, S. K. Chaubey and G. V. P. Kumar, *Adv. Opt. Mater.*, 2018, **6**, 1801025.
244 S. J. Peppernick, A. G. Joly, K. M. Beck and W. P. Hess, *J. Chem. Phys.*, 2012, **137**, 014202.
245 H. Aouani, F. Deiss, J. Wenger, P. Ferrand, N. Sojic and H. Rigneault, *Opt. Express*, 2009, **17**, 19085.
246 L. Liang, D. B. L. Teh, N.-D. Dinh, W. Chen, Q. Chen, Y. Wu, S. Chowdhury, A. Yamanaka, T. C. Sum, C.-H. Chen, N. V. Thakor, A. H. All and X. Liu, *Nat. Commun.*, 2019, **10**, 1391.
247 J. Lumeau, M. Mivelle, T. Begou, H. Rigneault, J. Wenger, F. Bedu, S. Bidault, J. Berthelot, N. Bonod, M. F. García-Parajó, P. M. Winkler, J. Proust, R. Regmi and I. Ozerov, *Nano Lett.*, 2016, **16**, 5143–5151.
248 A. Campion and P. Kambhampati, *Chem. Soc. Rev.*, 1998, **27**, 241.
249 I. Alessandri and J. R. Lombardi, *Chem. Rev.*, 2016, **116**, 14921–14981.
250 S. M. Spillane, T. J. Kippenberg and K. J. Vahala, *Nature*, 2002, **415**, 621–623.
251 J. Ward and O. Benson, *Laser Photonics Rev.*, 2011, **5**, 553–570.
252 I. M. White, N. M. Hanumegowda, H. Oveys and X. Fan, *Opt. Express*, 2005, **13**, 10754.
253 S. H. Huang, X. Jiang, B. Peng, C. Janisch, A. Cocking, Ş. K. Özdemir, Z. Liu and L. Yang, *Photonics Res.*, 2018, **6**, 346.
254 S. Arnold, D. Keng, S. I. Shopova, S. Holler, W. Zurawsky and F. Vollmer, *Opt. Express*, 2009, **17**, 6230.
255 K. J. Yi, H. Wang, Y. F. Lu and Z. Y. Yang, *J. Appl. Phys.*, 2007, **101**, 063528.
256 I. Alessandri, N. Bontempi and L. E. Depero, *RSC Adv.*, 2014, **4**, 38152–38158.
257 G. M. Das, M. K. Parit, R. Laha and V. R. Dantham, in *AIP Conference Proceedings*, AIP Publishing LLC, 2016, vol. 1728, p. 020564.
258 A. Arya, R. Laha, G. M. Das and V. R. Dantham, *J. Raman Spectrosc.*, 2018, **49**, 897–902.
259 J. Wang, Q. Hao, Y. Yin, L. Ma and O. G. Schmidt, *Phys. Status Solidi*, 2019, **256**, 1800379.
260 X. Hu, P. Jiang, C. Ding, H. Yang and Q. Gong, *Nat. Photonics*, 2008, **2**, 185–189.
261 B. Born, J. D. A. Krupa, S. Geoffroy-Gagnon and J. F. Holzman, *Nat. Commun.*, 2015, **6**, 8097.
262 B. Born, S. Geoffroy-Gagnon, J. D. A. Krupa, I. R. Hristovski, C. M. Collier and J. F. Holzman, *ACS Photonics*, 2016, **3**, 1095–1101.
263 M. Hasan and J. J. Simpson, *Appl. Opt.*, 2013, **52**, 5420.
264 G. E. Artzner, *Opt. Eng.*, 1992, **31**, 1311.

265 K. W. Allen, F. Abolmaali, J. M. Duran, G. Ariyawansa, N. I. Limberopoulos, A. M. Urbas and V. N. Astratov, *Appl. Phys. Lett.*, 2016, **108**, 241108.
266 A. Darafsheh, A. Fardad, N. M. Fried, A. N. Antoszyk, H. S. Ying and V. N. Astratov, *Opt. Express*, 2011, **19**, 3440.
267 T. C. Hutchens, A. Darafsheh, A. Fardad, A. N. Antoszyk, H. S. Ying, V. N. Astratov and N. M. Fried, *J. Biomed. Opt.*, 2014, **19**, 018003.
268 T. C. Hutchens, A. Darafsheh, A. Fardad, A. N. Antoszyk, H. S. Ying, V. N. Astratov and N. M. Fried, *J. Biomed. Opt.*, 2012, **17**, 068004.
269 A. Lombardini, V. Mytskaniuk, S. Sivankutty, E. R. Andresen, X. Chen, J. Wenger, M. Fabert, N. Joly, F. Louradour, A. Kudlinski and H. Rigneault, *Light: Sci. Appl.*, 2018, **7**, 10.
270 Y. Dong, J. Qi, H. He, C. He, S. Liu, J. Wu, D. S. Elson and H. Ma, *Biomed. Opt. Express*, 2017, **8**, 3643–3655.
271 V. Ushenko, A. Sdobnov, A. Syvokorovskaya, A. Dubolazov, O. Vanchulyak, A. Ushenko, Y. Ushenko, M. Gorsky, M. Sidor, A. Bykov, I. Meglinski, V. Ushenko, A. Sdobnov, A. Syvokorovskaya, A. Dubolazov, O. Vanchulyak, A. Ushenko, Y. Ushenko, M. Gorsky, M. Sidor, A. Bykov and I. Meglinski, *Photonics*, 2018, **5**, 54.
272 V. A. Ushenko, M. I. Sidor, Y. F. Marchuk, N. V. Pashkovskaya and D. R. Andreichuk, *Quantum Electron.*, 2015, **45**, 265–269.
273 T. Liu, T. Sun, H. He, S. Liu, Y. Dong, J. Wu and H. Ma, *Biomed. Opt. Express*, 2018, **9**, 4413–4428.
274 P. N. Saeta, V. E. Ferry, D. Pacifici, J. N. Munday and H. A. Atwater, *Opt. Express*, 2009, **17**, 20975.
275 G. Yin, P. Manley and M. Schmid, *Sol. Energy*, 2018, **163**, 443–452.
276 E. Yablonovitch and G. D. Cody, *IEEE Trans. Electron Devices*, 1982, **29**, 300–305.
277 J. Grandidier, D. M. Callahan, J. N. Munday and H. A. Atwater, *Adv. Mater.*, 2011, **23**, 1272–1276.
278 Y. J. Jin, L. W. Chen, M. X. Wu, X. Z. Lu, R. Zhou and M. H. Hong, *Opt. Mater. Express*, 2016, **6**, 1114.
279 F. J. V. Valero and M. N. Vesperinas, in *AIP Conference Proceedings*, American Institute of Physics, 2012, vol. 1475, pp. 176–178.
280 F. J. Valdivia-Valero and M. Nieto-Vesperinas, *Opt. Express*, 2011, **19**, 11545.
281 W. Liu, X. Li, Y. Song, C. Zhang, X. Han, H. Long, B. Wang, K. Wang and P. Lu, *Adv. Funct. Mater.*, 2018, **28**, 1707550.
282 H. S. Patel, P. K. Kushwaha, M. K. Swami and P. K. Gupta, *J. Opt.*, 2015, **17**, 055005.
283 H. Barhom, A. Machnev, R. E. Noskov, A. A. Goncharenko, E. Gurvitz, A. S. Timin, V. A. Shkoldin, S. V. Koniakhin, O. Y. Koval, M. Zyuzin, A. S. Shalin, I. Shishkin and P. Ginzburg, *Nano Lett.*, 2019, **19**, 7062–7071.
284 S. Das, M. J. Hossain, S. F. Leung, A. Lenox, Y. Jung, K. Davis, J. H. He and T. Roy, *Nano Energy*, 2019, **58**, 47–56.
285 Y. Zhang, S. Chen, D. Hu, Y. Xu, S. Wang, F. Qin, Y. Cao, B. O. Guan, A. Miroshnichenko, M. Gu and X. Li, *Nano Energy*, 2019, **62**, 682–690.
286 S. Haque, M. J. Mendes, O. Sanchez-Sobrado, H. Águas, E. Fortunato and R. Martins, *Nano Energy*, 2019, **59**, 91–101.
287 M. Calcerrada, C. García-Ruiz and M. González-Herráez, *Laser Photonics Rev.*, 2015, **9**, 604–627.
288 E. Kim, M. D. Baaske, I. Schuldes, P. S. Wilsch and F. Vollmer, *Sci. Adv.*, 2017, **3**, e1603044.
289 X. Li, Z. Chen, A. Taflove and V. Backman, *Opt. Express*, 2005, **13**, 526.
290 C. M. Ruiz and J. J. Simpson, *Opt. Express*, 2010, **18**, 16805.
291 Z. Chen, A. Taflove, X. Li and V. Backman, *Opt. Lett.*, 2006, **31**, 196.
292 A. Heifetz, K. Huang, A. V. Sahakian, X. Li, A. Taflove and V. Backman, *Appl. Phys. Lett.*, 2006, **89**, 221118.
293 S. Yang, A. Taflove and V. Backman, *Opt. Express*, 2011, **19**, 7084.
294 L. Zhao and C. K. Ong, *J. Appl. Phys.*, 2009, **105**, 123512.
295 S.-C. Kong, A. V. Sahakian, A. Heifetz, A. Taflove and V. Backman, *Appl. Phys. Lett.*, 2008, **92**, 211102.
296 Y.-C. Li, H.-B. Xin, H.-X. Lei, L.-L. Liu, Y.-Z. Li, Y. Zhang and B.-J. Li, *Light: Sci. Appl.*, 2016, **5**, e16176.
297 P. Ghenuche, J. de Torres, P. Ferrand and J. Wenger, *Appl. Phys. Lett.*, 2014, **105**, 131102.
298 H. Yang, M. Cornaglia and M. A. M. Gijs, *Nano Lett.*, 2015, **15**, 1730–1735.
299 C. Xie, M. A. Dinno and Y. Li, *Opt. Lett.*, 2002, **27**, 249.
300 P. Jing, J. Wu, G. W. Liu, E. G. Keeler, S. H. Pun and L. Y. Lin, *Sci. Rep.*, 2016, **6**, 19924.
301 Y.-F. Chen, X. Serey, R. Sarkar, P. Chen and D. Erickson, *Nano Lett.*, 2012, **12**, 1633–1637.
302 C. Min, Z. Shen, J. Shen, Y. Zhang, H. Fang, G. Yuan, L. Du, S. Zhu, T. Lei and X. Yuan, *Nat. Commun.*, 2013, **4**, 2891.
303 C. S. Adams and E. Riis, *Prog. Quantum Electron.*, 1997, **21**, 1–79.
304 I. V. Minin, O. V. Minin, Y. Cao, Z. Liu, Y. E. Geints and A. Karabchevsky, *Sci. Rep.*, 2019, **9**, 12748.
305 Y. Li, H. Xin, X. Liu, Y. Zhang, H. Lei and B. Li, *ACS Nano*, 2016, **10**, 5800–5808.
306 Z. Li, J. Yang, S. Liu, X. Jiang, H. Wang, X. Hu, S. Xue, S. He and X. Xing, *Opt. Express*, 2018, **26**, 34665.
307 J. Wu, W. Zhang and J. Li, *AIP Adv*, 2017, **7**, 085316.
308 A. Shakhov, A. Astafiev and V. Nadtochenko, *Opt. Lett.*, 2018, **43**, 1858.
309 A. Kovrov, A. Novitsky, A. Karabchevsky and A. S. Shalin, *Ann. Phys.*, 2018, **530**, 1800129.
310 G. Gu, J. Song, M. Chen, X. Peng, H. Liang and J. Qu, *Nanoscale*, 2018, **10**, 14182.
311 H. Wang, J. Zhang, X. Wu and D. Shen, *Opt. Express*, 2019, **27**, 10472.
312 H. Wang, X. Wu and D. Shen, *Opt. Lett.*, 2016, **41**, 1652.
313 P. D. Sewell, S. V. Boriskina, S. V. Pishko and T. M. Benson, *J. Lightwave Technol.*, 2007, **25**, 2487–2494.
314 S. Deng, W. Cai and V. N. Astratov, *Opt. Express*, 2004, **12**, 6468.
315 I. Chremmos and N. Uzunoglu, *IEEE Photonics Technol. Lett.*, 2006, **18**, 1173–1175.
316 Z. Chen, A. Taflove and V. Backman, *Opt. Lett.*, 2006, **31**, 389.

317 J.-J. Li, J.-X. Wang and Y.-Z. Huang, *Opt. Lett.*, 2007, **32**, 1563.
318 B. M. Möller, U. Woggon and M. V. Artemyev, *Phys. Rev. B: Condens. Matter Mater. Phys.*, 2007, **75**, 245327.
319 S. Yang and V. N. Astratov, *Appl. Phys. Lett.*, 2008, **92**, 261111.
320 A. M. Kapitonov and V. N. Astratov, *Opt. Lett.*, 2007, **32**, 409.
321 K. W. Allen, A. Darafsheh, F. Abolmaali, N. Mojaverian, N. I. Limberopoulos, A. Lupu and V. N. Astratov, *Appl. Phys. Lett.*, 2014, **105**, 21112.
322 T. Mitsui, Y. Wakayama, T. Onodera, T. Hayashi, N. Ikeda, Y. Sugimoto, T. Takamasu and H. Oikawa, *Adv. Mater.*, 2010, **22**, 3022–3026.
323 A. Kumar Tiwari, R. Uppu and S. Mujumdar, *Appl. Phys. Lett.*, 2013, **103**, 171108.
324 A. Darafsheh, N. Mojaverian, N. I. Limberopoulos, K. W. Allen, A. Lupu and V. N. Astratov, *Opt. Lett.*, 2013, **38**, 4208.
325 M. Benyoucef, J.-B. Shim, J. Wiersig and O. G. Schmidt, *Opt. Lett.*, 2011, **36**, 1317.
326 Y. Li, X. Liu, X. Xu, H. Xin, Y. Zhang and B. Li, *Adv. Funct. Mater.*, 2019, **10**, 1905568.